Hydrodeoxygenation mechanism of Acetaldehyde on Ru(0001), RuO_2(110), and RuO_2/TiO_2(110) from first-principles investigations

A Thesis

Presented to

the Faculty of the Department of

Chemical and Biomolecular Engineering

University of Houston

In Partial Fulfillment

of the Requirements for the Degree

Master of Science

in Chemical Engineering

by

Byeongjin Baek

May 2013

Acknowledgments

First of all, I would like to express my special thanks to God for having made everything possible by giving me strength and courage to do this work. I also want to thank Dr. Lars Grabow, my advisor, for the encouragement, guidance, and patience he demonstrated during my study. I extend my gratitude to all my research teammates including, Hieu Doan, Arian Ghorbanpour, and Sashank Kasiraju. Sharing research experience smoothened my research progress. Last and most importantly, I would like to thank my wife, Soojung Kim, for always being there for me with the greatest support and encouragement.

Hydrodeoxygenation mechanism of Acetaldehyde on Ru(0001), RuO_2(110), and RuO_2/TiO_2(110) from first-principles investigations

An Abstract

of a

Thesis

Presented to

the Faculty of the Department of

Chemical and Biomolecular Engineering

University of Houston

In Partial Fulfillment

of the Requirements for the Degree

Master of Science

in Chemical Engineering

by

Byeongjin Baek

May 2013

Abstract

Hydrodeoxygenation (HDO) of acetaldehyde, a surrogate molecule for the ca. 400 oxygenates in bio-oil, is explored on Ru(0001), RuO_2(110), and a RuO_2/TiO_2(110) overlayer surface using periodic density functional theory. Under typical HDO reaction conditions, the oxide surfaces are partially reduced and have bridging hydroxyls. Upon additional hydrogen adsorption, these surfaces form oxygen vacancies, which play a key role for the adsorption of acetaldehyde. Subsequent acetaldehyde isomerization favors C-O scission and leads selectively to the formation of ethylene on both RuO_2 and RuO_2/TiO_2 surfaces. In contrast, decarbonylation (C-C scission) and carbon deposition is more likely to occur on the metallic Ru(0001) surface. Overall, the rutile RuO_2 and RuO_2/TiO_2 surfaces seem more promising for selective C-O bond breaking than the metallic Ru(0001) surface. A more detailed understanding of catalytic differences between metals and metal-oxides for HDO is necessary to develop novel catalysts that can lead to an increased utilization of biofuels.

Table of Contents

List of Figures

List of Tables

Chapter 1. Introduction

1.1 Catalytic Upgrading of Bio-oil to Transportation oil

Ever since crude oil has been discovered in the 19th century, this cheap liquid fuel source has rapidly boosted industrialization and has improved our quality of living. However, over the past few decades, concerns such as depletion of petroleum resources and greenhouse gas emissions have made it imperative to develop eco-friendly processes for sustainable fuel production [1]. To this end, bio-oils derived from biomass are at the focal point of studies for the development of alternative energy sources because it is the only currently sustainable energy source of organic carbon and generates significantly less greenhouse gas than that of current fossil fuels. Even the generated greenhouse gases could be offset, if efficient processes for bio-fuels production were developed [2].

According to U.S Department of Agriculture reports, sustainable biomass resources in the U.S are 1.3×10^9 metric tons per year including agricultural (72 % of total) and forest (28% of total) resources [3]. These amounts of biomass correspond to the amount of energy of ca. 3.8×10^9 boe (barrels of oil energy), which is almost half of the total energy consumption of the U.S per year (7.0×10^9 boe). The estimated worldwide raw biomass energy in 2050 will be approximately 79.0 $\times 10^9$ boe [3].

Although significant amounts of raw materials are available, the commercialization of bio-fuels derived from biomass is still far from being commercialized due to the difficulties of transportation to regional refineries and the instability of oxygenated compounds in the intermediate bio-oil. Hence, significant research efforts have focused on the development of processes related to bio-oil upgrading and integration with current refineries. Typical strategies (Fig. 1) for the production of bio-fuel from biomass involve a removal of oxygen in the form of CO_2 or H_2O through a hydro-treating process, and convert it into higher-density liquid fuel [3].

As shown in Fig. 1, the biomass treatments can be classified as gasification, pyrolysis or liquefaction, and hydrolysis. Among these, the only processes that mainly produce liquids in form of bio-oils relatively easily are pyrolysis and liquefaction. The residence time, heating rate, and temperature are the parameters that determine phase and composition of bio-oils. The pyrolysis process produces dark viscous bio-oils, which contain more than ca. 400 different oxygenated organic or inorganic compounds including acids, alcohols, aldehydes, esters, ketones, and aromatic compounds [4]. Mine et al. investigated the composition of bio-oils derived from pyrolysis of cellulose in 1997 (see Fig. 2) [3]. The dominant components of bio oil contain acid and aldehyde functional groups.

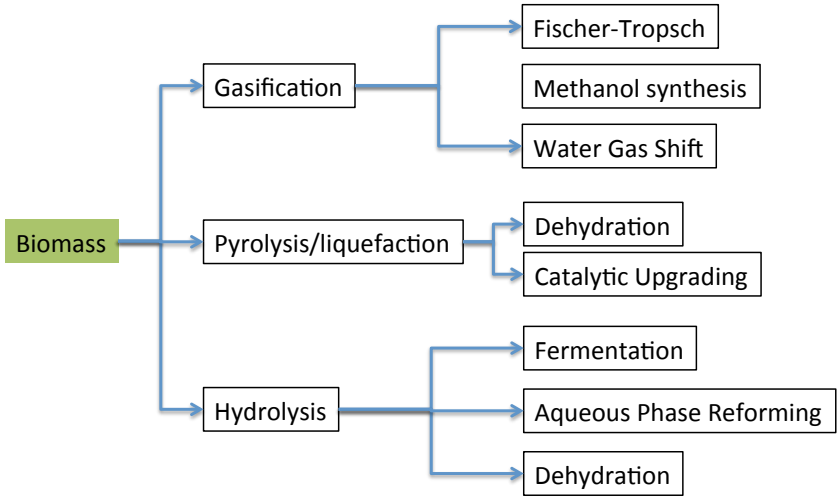

Fig. 1. Different strategies for the conversion of lignocellulosic biomass (taken from reference 4).

One of the main challenges for commercial use of bio-oils derived from pyrolysis is associated with the difficulties of oxygen removal from the 300 ~ 400 different oxygenated compounds, which lead to undesirable properties such as high viscosity, chemical instability, immiscibility with petroleum fuels, and low energy density [1]. To meet transportation fuel quality standards, bio-oil can be blended into the feed of petrochemical refineries or must be catalytically upgraded over zeolites or deoxygenation (DO) catalysts. Promoted sulfides, precious metals, and zeolites [5] are the most frequently studied types of catalyst for DO catalysis of organic molecules; some examples include HDO of aliphatic ester on NiMoS catalyst [6], HDO of guaiacol on transition

metal phosphide catalysts [7], HDO of furan on MoS_2 [8], and glycerol conversion over zeolites such as ZSM-5 and SAPO-11 [5, 9, 10]. DO catalysis can be generally separated into two categories: (i) hydrodeoxygenation (HDO), a process in which oxygen atoms are selectively removed as H_2O from oxygenated molecules in the presence of high pressure hydrogen gas leaving the number of carbon atoms constant; and (ii) decarbonylation (DCN) / decarboxylation (DCX), in which oxygen is removed in the form of CO and CO_2, respectively.

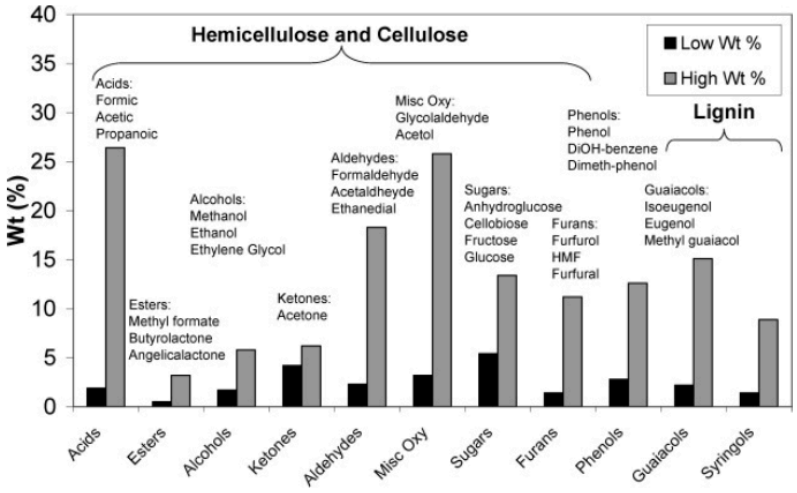

Fig. 2. Composition of bio-oils after pyrolysis of lignocellulosic biomass (taken from reference 3).

The selectivity between HDO versus DCN/DCX depends primarily on the catalyst's tendency for preferentially breaking C–O or C–C bonds in oxygenated molecules. For the production of liquid fuels from bio-oil it is clearly desirable to maintain the carbon content of the reactant species and only break C-O bonds via the HDO process. Because bio-oils are composed of many different organic molecules such as aldehydes, ketones, furans, phenolic compounds, guaiacol, syringol, and sugars, as shown in Fig. 2, there are numerous experimental studies on several oxygenated model molecules [8, 11–14]. However, there is currently no general consensus regarding the type of oxygen functionality that is most representative for DO studies of typical bio-oil feeds. It has been suggested that prior to the HDO treatment of bio-oil, the existing oxygen functionalities can be used to make intermediates with longer hydrocarbon chains to improve the

quality of the resulting fuel and simultaneously eliminate existing oxygen without any additional hydrogen requirements [15, 16]. One such example is the ketonization reaction between two carboxylic acids on reducible oxide catalysts, in which a total of three oxygen atoms are eliminated as CO_2 and H_2O. In the subsequent HDO step, only one oxygen atom must be removed from the ketone group using H_2 to produce an oxygen free hydrocarbon. While the oxygen atom of a ketone, or the closely related aldehyde group, is not as difficult to remove as for example the O atom in a furan ring, we suggest that aldehydes and ketones are suitable surrogates for initial DO studies, because these functionalities are present in large quantities and have neighboring C=O and C-C bonds that allow studies of the HDO selectivity.

Over a past decades state-of-art computational techniques have been successfully applied for many heterogeneously catalyzed reactions of small molecules such as CO/NO oxidation, ammonia synthesis [17, 18], and methanol synthesis [19], but the applications to biomass derived molecules were confronted with big challenges caused by the plethora of reaction pathways, the sheer size of biomass molecules, and the presence of solvents. Even to date, there are relatively few theoretical studies related to DO reactions of bio-oil compounds and previous work in this area is limited to propanoic acid on Pd(111) [20], furfural conversion to furan on Pd(111) [21], and a mechanistic DO study on Ni-promoted MoS_2 bulk catalysts [22]. Recent progress in density functional theory (DFT) calculation and rapidly increasing computational capabilities have enabled us now to study DO catalysis not just for small bio-oil molecules at the atomic-scale, but also for more complex molecules using a screening method [23], which can be extended for the design of new DO catalysts and the prediction of catalytic activity.

Here, hydrodeoxygenation (HDO) of acetaldehyde (CH_3COH), a major product of fast biomass pyrolysis, containing both a C-C bond and a C=O bond, is thoroughly studied by periodic DFT calculations on the Ru(0001) and the rutile $RuO_2(110)$ and $RuO_2/TiO_2(110)$ surfaces. Although Ru catalysts have poor catalytic activity under ultra high vacuum (UHV)

conditions, they are superior to Pt and Pd based catalysts under oxygen excess conditions, which are mainly attributed to a formed oxide layer over Ru metal surface. However, this phenomenon is still under debate because the formed RuO_2 overlayer is not active itself without metallic Ru present on the surface [24, 25]. Ru is further of interest, because it is highly active for hydrogenolysis of glycerol [26] and polymerized acetaldehyde decomposition [27], and RuO_2 has been indicated as the active phase for CO oxidation [28] and alcohol oxidation to ketone [29]. The focus of our study is to understand the mechanistic details of acetaldehyde HDO on Ru, RuO_2 and mixed RuO_2/TiO_2 and we want to specifically address the question of the order of bond activation in acetaldehyde (C-O, C=O, and C-H), which directly relates to the aforementioned DO selectivity. These results can be used to develop reactivity descriptors and guide the design of novel HDO metal or metal-oxide catalysts with desired DO properties.

1.2 Electronic Structure Theory

This chapter gives a brief summary of electronic structure calculations. We have used periodic density functional theory (DFT), which has become the state-of-the-art predictive tool for diverse materials modeling in chemistry, physics, materials science, and chemical engineering [30]. This is easily illustrated by performing a keyword search on the "*Science Citation Index*" for papers with the word "*Density Functional Theory.*" The citation index has increased by more than 100 times in 2012 compared to in 1996 [31]. This significant increase of DFT simulations in many areas of science and engineering is due to the fact that it can give us reasonable accuracy and predictive capability with acceptable computational requirements that are much less demanding than other simulation methods [32]. One of the main areas of interest in the recent literature are electronic structure calculations of solid-state systems that are relevant for heterogeneous catalysis and rational catalyst design. Readers who are interested in more detailed information about DFT are referred to read well-organized books and reviews [31, 32].

1.2.1 The Schrödinger Equation

The time-independent Schrödinger equation, which contains all quantum mechanical properties such as energy and position of nuclei and electrons of a system, is given by

$$\hat{H}\Psi = E\Psi, \tag{1}$$

where $\hat{H}$ is the Hamiltonian operator, Ψ is the many-particle wave function, and E is the total energy of the quantum mechanical system. The wavefunction $\Psi=\Psi(r_1,r_2,\ldots r_N)$ contains all information with respect to the internal degrees of freedom. Eq. (1) can be simplified by the Born-Oppenheimer approximation based on the large mass difference between the nuclei and electrons [33], i.e. each proton or neutron in a nucleus are 1800 times heavier than the mass of an electron. Hence, electrons are much more sensitive to changes in their surroundings than nuclei. As a result, we can solve eq. (1) assuming fixed positions of the nuclei and only describe the electrons' motion in the external potential determined by the positively charged nuclei. In other words, the degrees of freedom of the electrons can be decoupled from that of the nuclei. The approximated result for the Hamiltonian operator is then given by

$$\hat{H} = -\frac{1}{2}\sum_{i=1}^{N}\nabla_i^2 + \sum_{i=1}^{N}\sum_{J>i}^{N}\frac{1}{|r_j-r_i|} + \sum_{i=1}^{N}\sum_{i=1}^{N}\frac{Z_a}{|r_i-R_a|}, \tag{2}$$

where R is the position of the nuclei, r is the position of the electrons, and Z is the charge of the nuclei, respectively. Using the shorter form of notation, eq. (2) can be simplified as

$$\hat{H} = \hat{T} + \hat{V}_{ee} + \hat{V}_{ext}, \tag{3}$$

where first term, $\hat{T}$, is a kinetic energy of the electrons, the second term, $\hat{V}_{ee}$, is the repulsive interaction between the electrons, and the third term, $\hat{V}_{ext}$, is a attractive interaction between the fixed nuclei and the electrons, which can be conceptually interpreted as the interaction with an external potential caused by the fixed nuclei.

1.2.2 Density Functional Theory

DFT relies on two basic theorems proven by Kohn and Hohenberg that were further developed by Kohn and Sham in the 1960s. The idea behind DFT is that the electronic energy of a system

can be written in terms of the electron density, $\rho_{(r)}$, which reduces the problem of 3N degrees of freedom to 3 degrees of freedom, but contains the same energetic information as the full wave function of eqn. (1).

1.2.3 The Hohenberg-Kohn Theorem

The first Hohenberg-Kohn theorem states, "*The ground state energy from Schrödinger's equation is a unique functional of the electron density.*" Hence, it is possible to calculate the ground state energy corresponding to the ground state wave function, if the ground state electron density is known. The ground state energy can then be expressed as $\mathrm{E}[\rho_{(r)}]$, which is important because it allows equation (1) to be solved using only three spatial variables of the electron density rather than solving it with 3N degrees of freedom. This theorem, however, does not provide an exact mathematical definition of the functional form that related the energy to the electron density and it only proves that such a functional exists. The second Hohenberg-Kohn theorem states, "*The electron density that minimizes the energy of the overall functional is the true electron density corresponding to the full solution of the Schrödinger Equation.*" According to this theorem, if we can find the "*true*" functional, then the energy of the system can be minimized by variation of electron density (Variational Principle).

In summary, the Hohenberg-Kohn theorem can be simply expressed as a function of the electron density as given by the following equation,

$$\mathrm{E}\left[\rho_{(r)}\right] = \langle \Psi\left[\rho_{(r)}\right] | H | \Psi\left[\rho_{(r)}\right] \rangle, \tag{4}$$

$$= \mathrm{T}[\rho] + V_{ee}[\rho] + \int v(r)_{ext}\rho(r)dr, \tag{5}$$

$$= \mathrm{F}[\rho] + \int v(r)_{ext}\rho(r)dr\ , \tag{6}$$

where the functional is divided into a part that depends on the external potential, $\int v(r)_{ext}\rho(r)dr$, and a part which does not depend on the external potential, $\mathrm{F}[\rho]$. This expression is exact and is valid for a system with any number of particles and with any external potential, $v(r)_{ext}$. However, an analytical solution exists only for systems with one electron and

for systems of technical interest, iterative solution schemes must be employed. Hence, approximation and simplification must be made to enable the solution for larger systems while maintaining the accuracy of the result. This presents the major challenge for DFT calculations in practice.

1.2.4 The Kohn-Sham Equation

In 1965, Kohn and Sham (KS) presented an idea to approximate the solution to the many-body electronic structure problem. In their approach, the problem of interacting electrons is replaced with an independent particle system by assuming that the ground state density of the non-interacting system can represent the ground state density of interacting system by defining an appropriate effective potential, $v_{eff}(r)$. As a result, Hohenberg and Kohn suggest that the real electron density can be obtained from single electron wave functions, $\psi_i(r)$, and all the many body effects are grouped into an exchange correlation functional. Thus, the total energy functional of N electron can be given by

$$E[\psi_i] = E_{known}[\psi_i] + E_{xc}[\psi_i], \tag{7}$$

where the $E_{known}[\psi_i]$ is the collection of term we can calculate analytically and the $E_{xc}[\psi_i]$ is everything else including many body effects. The $E_{known}[\psi_i]$ is then expressed as

$$E_{known}[\psi_i] = -\frac{h^2}{m}\sum_i \int \psi_i^* \nabla^2 \psi_i d^3r + \int V(r)\,\rho(r) d^3r + \frac{e^2}{2}\iint \frac{\rho(r)\rho'(r)}{|r-r'|} d^3r d^3r' + E_{ion}, \tag{8}$$

where the first term represents the kinetic energies of the electrons, the second term represents Coulomb interactions between electrons and nuclei, the third term are Coulomb interactions between electron, and the last term represents Coulomb interactions between nuclei. The remaining term in eq. (7), $E_{xc}[\psi_i]$, is the exchange–correlation functional, which includes all the quantum mechanical effects that are not included in the "known" terms. The total electron density of the system can then be found from the one-electron wave functions given by

$$\rho(r) = 2\sum_{i=1}^{N} |\psi_i(r)|^2, \tag{9}$$

in which the factor 2 results from the spin up and down states according to Pauli's exclusion principle. The one-electron wave functions are obtained by solving the single particle Kohn-Sham (KS) equations as given by

$$\left[-\frac{h^2}{2m}\nabla^2 + V(r) + V_H(r) + V_{xc}(r)\right]\psi_i(r) = \varepsilon_i\psi_i(r), \tag{10}$$

where the first potential V describes interactions between an electron and the collection of atomic nuclei, the second potential is called Hartree potential and accounts for Coulomb repulsions between electrons, and the third term is the exchange-correlation potential. Since the single electron itself in equation (10) belongs to the total electron density, the Hartree potential should be corrected for self-interaction errors. Therefore, not only these unphysical interactions, but also many body effects, are grouped into the $V_{xc}(r)$, which is the functional derivative of the exchange-correlation energy, $E_{xc}[\rho(r)]$, as expressed as

$$V_{xc}(r) = \frac{\delta E_{xc}[\rho(r)]}{\delta\rho(r)}. \tag{11}$$

1.2.5 The Exchange-Correlation

Finding an accurate exchange-correlation functional is the main challenge for DFT calculations as mentioned earlier, and several empirical and semi-empirical functionals with different strengths and weaknesses have been proposed. The most commonly used approximations in solid-state physics are the Local Density Approximation (LDA) and the Generalized Gradient Approximation (GGA). The LDA functional uses only the local density of a uniform electron gas. On the other hand, the GGA takes into account both the local electron density and the local gradient of the electron density. However, it is not necessarily always the case that the GGA is more accurate than the LDA, only because the GGA contains for more physical information. In this thesis, a GGA functional based on the revised Perdew-Burke-Ernzerhof (RPBE) functional [34] is rigorously applied, which has been shown to give a good description of the energetics for adsorbed species on surfaces.

1.2.6 Self-Consistent-Field Cycle

In order to solve the KS equations self-consistently, an iterative method must be applied. This iterative method is called the Self-Consistent Field (SCF) Cycle. The cycle is terminated when a pre-defined convergence criterion for changes in the electron density is met. The cycle can be described as follows:

1. Guess the trial electron density, $\rho(r)_{trial}$.
2. Apply the $\rho(r)_{trial}$ in the KS equations and solve for the single-electron wave functions, $\psi_i(r)_{initial}$.
3. Plug in equation (9) to find the KS electron density, $\rho(r)_{KS}$.
4. Compare $\rho(r)_{KS}$ to $\rho(r)_{trial}$ and if the two densities are equal, this is the ground state electron density. This electron density can then be used to compute the total energy. If the densities are not equal, go back to step 1 with an updated $\rho(r)_{trial}$.

A full description of the solution strategy is illustrated in reference [32].

1.3 Equilibrium Surface Phase Diagrams From DFT Calculations

Results from DFT calculations are obtained at zero pressure and temperature, i.e., all physical quantities are strictly only valid at zero T and p. In reality, however, all relevant processes occur at finite p and T. It is certainly important to extend DFT results to more practically relevant conditions. In order to account for finite T and p in DFT calculations, the Gibbs free energy (G),

$$G(T,p) = \mathrm{E}^{\mathrm{tot}} - TS^{conf} + pV, \tag{12}$$

should be evaluated as a function of the T and p of interest. In eq. (12), the first term, $\mathrm{E}^{\mathrm{tot}}$, corresponds to the internal energy, the second term, TS^{conf}, is the configurational entropy, and the third term is pV-contributions. The $\mathrm{E}^{\mathrm{tot}}$ is more specifically given by

$$E^{tot} = E^{elec} + E^{ZPE} + \int_0^T C_p dT = E^{elec} + F^{vib}, \tag{13}$$

where the E^{elec} is directly obtained from electronic structure calculation, and the F^{vib} is the vibrational free energy.

In equilibrium, a bulk material surrounded by gas phase molecules can be described by its internal energy (E), which depends on the entropy (S), the volume (V), and the number of particles (N), as expressed in

$$E^{bulk} = TS - pV + \sum_i N_i \mu_i(T,p), \tag{14}$$

where the $\mu_i(T,p)$ is the chemical potential of species *'i'*. When surfaces are considered, we also need to consider the surface free energy, $\gamma(T,p)$, which describes the work necessary to create the surface

$$E^{surf} = TS - pV + \sum_i N_i \mu_i(T,p) + A\gamma(T,p). \tag{15}$$

In equation (15) A is the surface area. Since the Gibbs free energy is given by eq. (12), the eq. (15) can be rearranged by

$$\gamma(T,p) = \frac{1}{A}\left[G^{surf}(\mathrm{T,p}) - \sum_i N_i \mu_i(T,p)\right], \tag{16}$$

where G^{surf} is the Gibbs free energy of the surface. Again, μ_i is the chemical potential of species *'i'*, which is directly evaluated by T and p as given by

$$\mu_i = \mu_i^{\circ}(T,p^{\circ}) + kTln(^{p_i}/_{p_i^{\circ}}). \tag{17}$$

The superscript 'o' denotes a reference pressure, usually taken to be 1 bar. To calculate $\gamma(T,p)$ we need to express $G^{surf}(\mathrm{T,p})$ in terms of corresponding DFT energies. The leading term of $G^{surf}(\mathrm{T,p})$ on the right hand side of eq. (12) is the total electronic energy, E^{elec}, which is easily obtained from DFT calculations. The remaining terms (F^{vib}, S^{conf}, pV) can typically be neglected, because their contributions are orders of magnitude smaller as shown next.

First, the pV-term can be approximated by a simple dimensional analysis. Since the dimension of the surface free energy is per unit area [Å^2], the calculated pV-term will be roughly given by

$$[\mathrm{pV/Area}] = [\mathrm{bar}\times\text{Å}^3 / \text{Å}^2] = [10^{-25}\ \mathrm{J}/\text{Å}^2] \approx [10^{-3}\ \mathrm{meV}/\text{Å}^2]. \tag{18}$$

This means that even up to 100 bar the pV-contribution is much less than 0.1 meV/Å^2, which is extremely small. Therefore, the pV-contribution can be safely neglected. Second, the configurational entropy, which strongly depends on the accessible degrees of freedom of the

surface that we are interested in, can also be neglected under the assumptions that the surface is a well-ordered crystal or metal oxide. According to statistical mechanics, the configurational entropy contribution for a system with 'N' surface sites and 'n' defects sites is given by

$$S^{conf} = k_b \ln \frac{(N+n)!}{N!n!}. \quad (19)$$

With the assumption that the ratio (n/N) stays within 10 %, equation (19) can be rewritten as

$$\frac{TS^{conf}}{A} \leq 0.34 \frac{k_b T}{Area\ of\ one\ site}. \quad (20)$$

From eq. (20) and temperatures up to 1000 K (assuming that the surface area per one site ≈ 20 Å^2, if we use radius of Ru atom) the configurational entropy will at most contribute 6.0 meV/Å^2 to $G^{surf}(\mathrm{T,p})$. It is, however, important to note that this approximation will not be valid for highly disordered surface phases. The last term, the vibrational contribution to the free energy, F^{vib}, is not easy to evaluate, because it requires the full phonon density of state (PDOS) of the surface and the bulk. This is a time consuming procedure, but we may assume that the phonon frequencies of the bulk and the surface are similar and can therefore ignore this vibrational contribution as well. Changing the characteristic frequencies for bulk atoms by ± 50 % does not change the order of magnitude of vibrational contributions significantly. This result makes it clear that even up to 1000 K the vibrational contribution to the surface free energy is quite moderate. In conclusion, the contribution of E^{tot} to $G^{surf}(\mathrm{T,p})$ is the most dominant one and the other remaining terms (F^{vib}, S^{conf}, pV) may be neglected in a first order approximation. However, we should carefully test this assumption for every new system.

Chapter 2. Computational Details

2.1 General Methodology

All density functional theory (DFT) calculations (adsorption energies, activation energy barriers and vibrational frequencies) reported here have been calculated using the Vienna Ab-initio Simulation Package (VASP) in combination with the Atomic Simulation Environment (ASE) [35, 36]. The revised Perdew – Burke – Ernzerhoff - generalized gradient approximation (RPBE - GGA) was used as exchange-correlation functional [34, 37]. The interactions between core and valence electrons were represented by the projected augmented wave (PAW) method and the cut-off energy of 400 eV for plane wave was selected for this study. With the exception of gas phase molecules, a Fermi temperature of k_BT = 0.1 eV was used for all calculations and the resulting energies were extrapolated to zero electronic temperature [19]. For gas phase species k_BT = 0.01 eV was chosen.

The conjugated gradient algorithm with a force convergence criterion of 0.05 eV/Å was used for ionic relaxations of equilibrium geometries. The optimized bulk lattice constants are a = 2.689 Å, c/a = 1.637 for the Ru, a = 4.589 Å, c/a = 0.686, u = 0.306 for the RuO_2, and a = 4.723 Å, c/a = 0.629, u = 0.306 for the TiO_2, which are in good agreement with experimental data [38, 39]. The slabs consist of four atomic layers using a p(3 × 3) surface unit cell for Ru(0001) and a p(3 × 2) surface unit cell for RuO_2(110) and RuO_2/TiO_2(110). For all systems, the top two layers are fully relaxed and the bottom two layers are fixed at their bulk positions.

To avoid interaction between successive slabs due to the periodic boundary conditions, the unit cell included 20 Å of vacuum along the normal direction of the surface. A dipole correction was applied to compensate the effect of adsorbing molecules only on one side of each surface. The Brillouin zone was sampled using a (8×8×1) k-point grid for the Ru(0001) surface and a

(6×8×1) k-point grid for the RuO_2(110) and RuO_2/TiO_2(110) surfaces using the Monkhorst-Pack scheme [40].

2.2 Binding Energy Calculations

Binding energies (E_{BE}) are calculated with respect to the clean surface and the gas phase molecules (H_2, H_2O, CH_4, CH_3CHO) as given by

$$E_{BE} = E_{slab+adsorbate} - (E_{slab} + E_{molecule}). \quad (21)$$

The $E_{slab+adsorbate}$ is the total energy of the surface with adsorbates, E_{slab} is the energy of RuO_2(110), RuO_2/TiO_2(110) or Ru(0001), and $E_{molecule}$ is the gas phase reference energy of the appropriate gas phase molecules. A negative value of the E_{BE} means favorable adsorption with respect to the chosen gas-phase reference species.

2.3 Calculation of Activation Energies and Verification of Transition States

The climbing image nudged elastic band (cNEB) method, which is the most widely used method for finding transition states (TS) on complex potential energy surfaces (PES), was implemented to determine the TS of reaction pathways. A total of five or six interpolated images was used to sample the reaction pathway and the images were fully relaxed until the force criterion of 0.1 eV/Å was reached. The cNEB is an extension of the NEB method and forces the image with the highest energy to move up along the PES to the top of the minimum energy pathway (MEP). Once a calculation is converged, the energy difference of the image corresponding to the TS within the PES and the initial state (IS) gives the activation energy barrier (E_a) of the reaction pathway. For the determination of the MEP between an initial state (IS) and final state (FS) the geometries of the IS and FS must be provided as input to the NEB algorithm. The execution of the NEB algorithm requires evaluations of total energies and the corresponding first derivatives of the energy with respect to the coordinate of each image (force). Furthermore, NEB calculations can be highly parallelized, because the evaluation of the total energy of each intermediate image can be performed independently and requires little

communication between computing nodes. In order to locate the TS, the energy and gradient need to be evaluated for each image. Then for each image, the coordinates of two adjacent images are required to estimate the local tangent along the reaction path in order to project forces onto the perpendicular component of the gradient and combine with the parallel component of the spring force according to

$$F_i = \mathrm{F}_\mathrm{i}^{\perp} + \mathrm{F}_\mathrm{i}^{s}, \tag{22}$$

where $\mathrm{F}_\mathrm{i}^{\perp}$ is the force perpendicular to the path and the $\mathrm{F}_\mathrm{i}^{s}$ is the parallel component of spring forces, respectively. Vibrational analysis on all TS structures was performed to verify the existence of a single imaginary mode (saddle point), corresponding to the reaction coordinate along the reaction path.

Chapter 3. Results and Discussion

3.1 HDO of CH_3CHO on $RuO_2(110)$

3.1.1 Thermodynamic $RuO_2(110)$ surface phase diagram and vacancy formation kinetics under HDO conditions

It is generally accepted that on the stoichiometric $RuO_2(110)$ surface coordinatively unsaturated Ru atoms, referred to as the Ru^{cus} site, form the preferred adsorption site for small molecules such as CO, O_2, N_2O and CH_3CHO with fairly high adsorption energies (≤ -0.7 eV) because of its localized electronic properties [29, 41, 42]. However, at elevated temperature and pressure conditions under which all practical catalysis is performed the active oxide surface may significantly deviate from the stoichiometric $RuO_2(110)$ surface. Hence, it is necessary to bridge the zero pressure/temperature conditions with practical HDO reaction conditions that can lead to partial surface reduction and vacancy formation through hydrogen adsorption and subsequent water desorption. Here, we consider typical HDO reactions that are conducted under high-pressure of hydrogen and high-temperature (T > 400 K and P_{H2} > 200 bar). Under these reaction conditions, surface modification by adsorption of H_2 and desorption of H_2O from the surface are driven by minimization of the surface free energy (γ), which solely depends on the chemical potential of H_2O (μ_{H_2O}) and H_2 (μ_H) as given by [43]

$$\gamma(T,p) = {}^{1}/_{2A}\left[E_{slab} - N_{Ru}E_{RuO_2}^{bulk} + (2N_{Ru} - N_O)\mu_{H2O} - 2\big((2N_{Ru} - N_O) + N_H\big)\mu_H\right], \quad (23)$$

where the A is the surface area, E_{slab} is total energy of the surface slab and the chemical potential of H_2 and H_2O are simply calculated from tabulated table. [44, 45]. Plotting the surface phase with the lowest surface free energy for given values of μ_{H_2O} and μ_H leads to a thermodynamic phase diagram that is capable of predicting stable surface phases for given temperatures and partial pressures [43, 46]. The most stable $RuO_2(110)$ surface under specified HDO conditions (600 K and 200 bar of hydrogen; μ_H = -0.18, μ_{H2O} = 0.01) is a partially hydrogenated surface on which all bridging oxygen atoms (O^{br}) are hydrogenated (see S. 1 in

Appendix). The dissociative adsorption of H_2 and formation of two neighboring O^{br}-H groups on the surface is exothermic with ΔE = -1.85 eV. These results are in agreement with experimental data [47, 48] suggesting that atomic and molecular hydrogen prefer to adsorb on the O^{br} site and the Ru^{cus} site. This is further supported by DFT calculations by Knapp *et al.* investigating the binding energy for various hydrogen adsorption geometries over RuO_2(110) [49]. It was further suggested that if there is no additional oxygen on the Ru^{cus} site, hydrogen either adsorbs weakly on the Ru^{cus} site or strongly binds on the O^{br} site, forming a H_2O-like surface intermediate referred to as dihydride [50]. This dihydride is stable only below 90 K and upon heating the release of atomic hydrogen is observed followed by adsorption to an unoccupied O^{br} site, forming bridging hydroxyl. In addition, H_2O can be desorbed from this surface by combination of two neighboring bridging hydroxyl groups (Ru-O-H^{br} + Ru-O-H^{br} → $H_2O_{(g)}$ + Ru-O^{br} + Ru-vacancy) at even higher temperature (> 550 K), leaving oxygen vacancies behind on the surface.

Vacancy formation is considered an important step for catalysis on metal-oxide surfaces, because it plays key role for the adsorption of adsorbates. Therefore, the vacancy creation process is believed to be directly related to the catalytic activity of metal-oxide catalysts [30]. There is ample experimental evidence showing that metal-oxides can form vacancies under high-pressure of hydrogen, however, the vacancy formation mechanism and the kinetics under realistic conditions are not completely understood. To the best of our knowledge, this is the first comprehensive DFT study for vacancy formation on the RuO_2(110) surface with considerations of both kinetics and thermodynamics of multiple formation pathways under HDO conditions.

There are many possible pathways for vacancy formation. Firstly, H_2O can be generated via the pathway suggested by Ertl's group under UHV conditions, *i.e.,* disproportionation of two adjacent bridging hydroxyls (reaction O1 in Table 1) [50]. The initial state (IS) is the fully hydroxylated RuO_2(110) surface, termed RuO_2-3H here, and the final state (FS) has one empty O^{br} site and H_2O* on the surface as shown in Fig 1(a). At the TS, the distances between O^{br} and H,

$d_{\text{O-H*-OH*}}$, are 1.180 Å (O^{br}-H*) and 1.321 Å (H*-O^{br}H*). The calculated E_a and ΔE are 1.15 eV and 1.00 eV, respectively. The desorption energy of the formed H_2O* is 0.43 eV.

Table 1. List of elementary steps in the main reaction pathway for O-vacancy formation and HDO of CH_3CHO on the RuO_2(110) surface.

no.	Reaction	E_{BE}^{IS}	E_{BE}^{FS}	E_a	ΔE	ν
O0[a]	$H_{2(g)} + 2O^{br} \rightarrow$ O-2H^{br}*	.	.	.	-1.85	.
O1	O-H^{br}* + O-H^{br}* → H_2O^{br}* + O^{br}	-2.64	-1.64	1.15	1.00	1041.8i
O2	Ru-H_2^{cus}* + O^{br} → Ru-H^{cus}* + O-H^{br}*	-1.96	-2.54	0.29	-0.57	870.1i
O3	Ru-H^{cus}* + O-H^{br}* → Ru^{cus} + H_2O^{br}*	-2.54	-2.28	0.93	0.26	783.6i
O4[b]	$CH_3CHO_{(g)} \rightarrow CH_3CHO$*	.	.	.	-0.23	.
O5[c]	CH_3CHO*-s → CH_3CHO*-d	-0.23	-0.45	0.06	-0.22	160.5i
O6	CH_3CHO*-d + Ru^{cus} → Ru-CH_3CH^{cus}* + O^{br}	-0.45	0.14	0.83	0.59	243.3i
O7	Ru-CH_3CH^{cus}* + O^{br} → Ru-CH_2CH^{cus}* + O-H^{br}*	0.14	-0.29	0.52	-0.43	976.9i
O8	Ru-CH_2CH^{cus}* + O-H^{br}* → $CH_2CH_{2(g)}$ + O^{br}	-0.29	-0.14	0.85	0.15	1220.9i
O9[d]	$H_{2(g)}$ + O^{3f} + O-H^{br}* → O-H^{3f}* + H_2O^{br}*	.	-0.30	.	-0.01	.
O10	Ru-CH_2CH^{cus}* + O-H^{3f}* → Ru^{cus} + $CH_2CH_{2(g)}$	-0.30	-0.62	0.82	-0.32	1298.4i
O11[e]	H_2O^{br}* → $H_2O_{(g)}$	.	.	.	0.32	.

- E_{BE}^{IS}, E_{BE}^{FS}, E_a, and ΔE are in eV.
- E_{BE} is the binding energy of surface intermediates referenced to the $RuO_{(2-x)}$(110) surface and the gas phase molecules (H_2, H_2O, CH_3CHO, and CH_4) except for O0, which is referenced to the stoichiometric RuO_2(110) surface. Superscripts IS and FS are acronyms of initial and final state.
- ν denotes the frequency of the imaginary mode at the transition state in cm^{-1}.
- ΔE and E_a are the total energy change and activation energy barriers without ZPE correction.
- [a] O0 is the dissociative H_2 adsorption on the stoichiometric RuO_2(110) surface.
- [b] O4 is the adsorption of CH_3CHO on the O-vacancy site.
- [c] O5 is the isomerization of the CH_3CHO-s intermediate.
- [d] O9 is H_2 adsorption.
- [e] O11 is H_2O desorption at the end of catalytic cycle.

Another possible pathway (reactions O2 and O3 in Table 1) for H_2O formation is shown in both Fig. 3(b) and (c) and involves two consecutive hydrogenation steps. At the beginning of the reaction, hydrogen adsorbs molecularly with -0.11 eV on the Ru^{cus} site, forming Ru^{cus}-H_2*, as shown in the IS of Fig. 3(b). As mentioned before, atomic and molecular hydrogen were both shown to adsorb on the Ru^{cus} site in experimental observations and by DFT calculations [47, 48, 51]. The diatomic bond length $d_{\text{H-H}}$ of the hydrogen molecule (0.748 Å) is elongated to 0.791 Å upon adsorption on the Ru^{cus} site due to hybridization of Ru-d_{z^2} with H_2-σ orbitals, whereby a small amount of charge transfers from hydrogen to the Ru^{cus} site [47]. This strengthens the Ru^{cus}-H_2* bond while weakening the H-H bond [48]. During reaction O2 in Table 1, H_2* can be easily activated and dissociated, whereby one H atom diffuses to the empty O^{br} site. At the TS, the bond

lengths $d_{RuH^*-H^*-O}$ are 0.926 Å (RuH^{cus}*-H*O^{br}) and 1.495 Å (H*-O^{br}), which are consistent with other DFT data[37]. The calculated ΔE and E_a for reaction O2 in Table 1 are -0.58 eV and 0.29 eV, respectively. This indicates that reaction O2 is expected to be feasible even at low temperature. The hydrogen atom remaining on the Ru^{cus} site after the initial H_2 activation can subsequently transfer to the same bridging hydroxyl, forming H_2O* at the bridge site as shown in Fig. 3(c). The IS is similar to the IS of reaction O1, with the exception that there is one extra hydrogen atom on the Ru^{cus} site. At the TS, d_{Ru-H^*-O} are 1.748 Å (Ru^{cus}-H*) and 1.433 Å (RuH^{cus}*- H*O^{br}). The calculated ΔE and E_a are 0.26 eV and 0.93 eV, respectively. The desorption of formed H_2O* is endothermic by 0.25 eV allowing for facile vacancy creation on the surface.

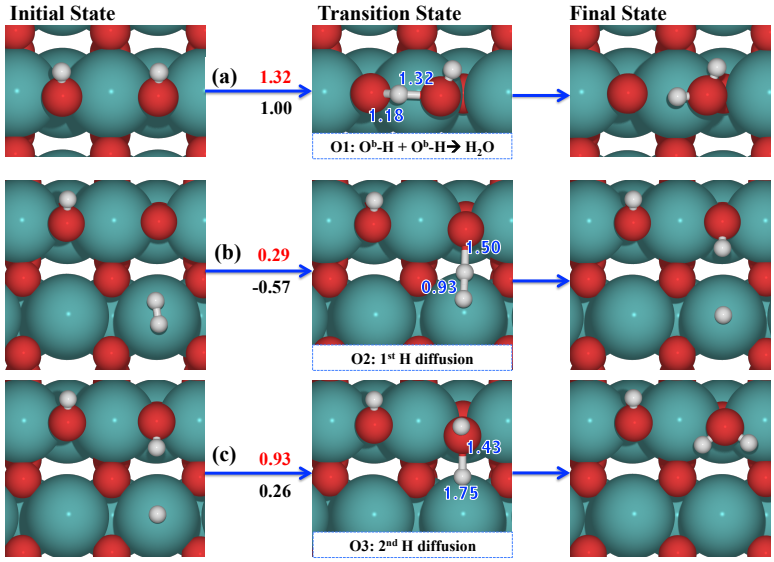

Fig. 3. Calculated reaction pathways for O-vacancy formation (white – hydrogen / red – oxygen / gray – carbon / teal – ruthenium). Numerical values in red, black and blue represent the activation energy barrier E_a [eV], the reaction energy ΔE [eV] and bond distance [Å], respectively. (a) Reaction O1: O-H^{br}* + O-H^{br}* → H_2O^{br}* + O^{br}; (b) Reaction O2: Ru-H_2^{cus}* + O^{br} → Ru-H^{cus}* + O-H^{br}*; (c) Reaction O3: Ru-H^{cus}* + O-H^{br}* → Ru^{cus} + H_2O^{br}*.

In addition to these two H_2O formation pathways, we have also considered two Eley-Rideal type reaction pathways: (i) dissociative hydrogen adsorption on the same O^{br} site leading directly to H_2O*, and (ii) dissociative hydrogen adsorption on two neighboring O^{br} sites (see Appendix S.2). However, both cases are unlikely due to high activation barriers (> 2.0 eV).

The feasible reaction pathways for vacancy formation can be summarized as follows:

Via reaction O1: $RuO_2 + 3/2H_{2(g)} \rightarrow RuO_{(2-x)} + H_2O_{(g)} + H^*$ [ΔE=-1.22 eV / E_a=1.15 eV], (24)

Via reactions O2+O3: $RuO_2 + 2H_{2(g)} \rightarrow RuO_{(2-x)} + H_2O_{(g)} + 2H^*$ [ΔE=-2.03 eV / E_a=0.93 eV]. (25)

Here, $RuO_{(2-x)}$ denotes the RuO_2 surface with a surface vacancy. Therefore, our results show that under high hydrogen pressures that allow for the adsorption of additional H_2 on the Ru^{cus} site, vacancy formation is kinetically and thermodynamically feasible through the reactions O2 and O3 in Table 1.

3.1.2 HDO pathways of CH_3CHO on the vacancy site of RuO_2(110)

Given that a vacancy on RuO_2(110) is available, CH_3CHO can adsorb on this vacancy site through the interaction of oxygen of the formyl group (HC=O) of CH_3CHO with E_{BE} of -0.23 eV, forming a single bonded precursor CH_3CHO*-s. Upon adsorption, $d_{C\text{-}O}$ of CH_3CHO* is slightly elongated by 3 % to 1.26 Å, whereas $d_{C\text{-}C}$ is kept essentially constant compared to gas phase CH_3CHO. The CH_3CHO*-s specie can be transformed into a more energetically favorable structure by isomerization (reaction O5 in Table 1), leading to CH_3CHO*-d with E_{BE} of -0.45 eV as shown in Fig. 4(a). The more stable adsorption geometry is often called a bidentate configuration where both the αC and oxygen of CH_3CHO* are interacting with the surface (αC-Ru^{cus} and O-Ru^{br}). At the TS, $d_{O^*\text{-}C^*\text{-}Ru}$ are 1.304 Å (O*-αC*) and 2.925 Å (αC*-Ru^{csu}). The calculated E_a and ΔE of this isomerization are 0.06 eV and -0.22 eV, which are energetically and kinetically feasible even at very low temperatures. An interesting observation regarding the bond distances during the isomerization can be made. The bond distances of the bidentate configuration are 1.392 Å (αO*-C) and 1.520 Å (αC*-C). A comparison of these values to those of gas phase CH_3CHO shows that the $d_{O^*\text{-}C^*}$ is increased by 18 %, while the $d_{C^*\text{-}C}$ is approximately constant. Since bond lengths can be taken as a first order approximation as a measure of bond strength, this indicates that the strength of the αC-O bond is weakened as CH_3CHO*-s transforms into CH_3CHO*-d. Yong. *et al.* recently published similar results for CH_3CHO adsorption on MoO_3

[52] where they refer to the bidentate configuration as a doubly bonded structure that is also more stable than the singly bonded CH_3CHO*-s configuration.

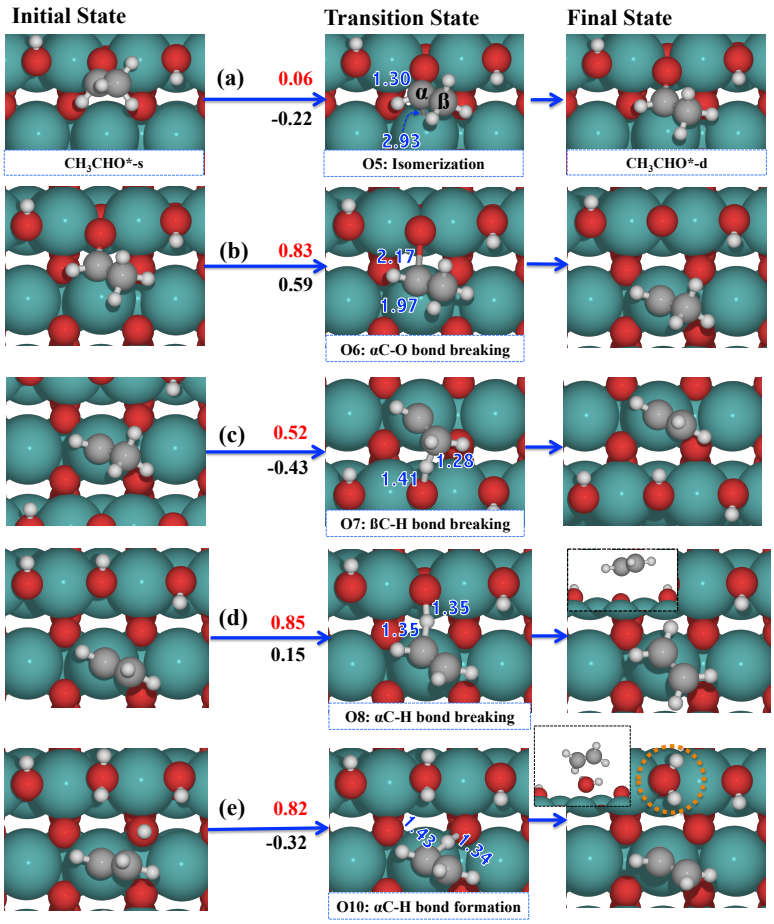

Fig. 4. Calculated reaction pathway of CH_3CHO HDO on RuO_2(110) (white – hydrogen / red – oxygen / gray – carbon / teal – ruthenium). Numerical values in red, black and blue represent the activation energy barrier E_a [eV], the reaction energy ΔE [eV] and bond distance [Å], respectively. (a) Reaction O5: CH_3CHO*-s → CH_3CHO*-d, isomerization; (b) Reaction O6: CH_3CHO*-d → Ru-CH_3CH^{cus}* + O^{br}; (c) Reaction O7: Ru-CH_3CH^{cus}* + O^{br} → Ru-CH_2CH^{cus}* + O-H^{br}*; (d) Reaction O8: Ru-CH_2CH^{cus}* + O-H^{br}* → O^{br} + $CH_2CH_{2(g)}$; (e) Reaction O10: Ru-CH_2CH^{cus}* + O-H^{3f}* → O^{3f} + $CH_2CH_{2(g)}$ - water is indicated by the orange circle.

Next, we focus on the possible elementary reactions that are possible for each reaction intermediate starting from CH_3CHO*. We have investigated at total of 30 elementary steps, but we limit our discussion to the most feasible pathways obtained by assuming that the reaction follows the path of least resistance, *i.e.,* we eliminate pathways that involve large activation barriers. The complete list of investigated steps in given in Table S1 in the Appendix. For CH_3CHO*-d there are four different possible bond breaking steps (C-C, αC-H, ßC-H, αC-O).

Among them, the αC-O bond scission (reaction O6 in Table 1) has the lowest E_a of 0.83 eV as shown in Fig. 4(b). The competing C-H bond scission reaction have similar activation barriers (0.90 eV) but these pathways lead to CH_3CO* and CH_2CHO* intermediates that require overcoming much larger barriers in subsequent steps. The C-C bond breaking step in CH_3CHO*-d has a considerably larger barrier (1.46 eV) and is not considered further.

A summary of all investigated elementary steps is shown in Table S1 in the Appendix. For comparison, we have also investigated the four decomposition pathways (C-C, αC-H, ßC-H, αC-O) which start from CH_3CHO*-s (see Table S1 in the Appendix). The E_a of the C-C and two C-H bond breaking are much higher than that of the αC-O bond breaking in CH_3CHO*-d. The αC-O bond breaking pathway proceeds only after isomerization to the bidentate configuration and an E_a from CH_3CHO*-s could not be obtained.

As an alternative to the decomposition pathways, we investigated the intramolecular hydrogen diffusion pathway (CH_3CHO*-s → $CH_2CH_{2(g)}$ + O^{br}*), which is the most direct pathway for ethylene (CH_2CH_2) formation, but with a barrier of E_a = 2.18 eV this step is kinetically hindered and can be eliminated (see Table S1 in the Appendix). The calculated ΔE of αC-O bond activation in CH_3CHO*-d (reaction O6) is endothermic by 0.59 eV. At the TS, $d_{O\text{-}C}$ is elongated from 1.392 Å to 2.170 Å. After the αC-O bond breaking, the ethylidene (CH_3CH*) intermediate adsorbs on the Ru^{cus} site with E_{BE} = 0.14 eV and the oxygen vacancy on $RuO_{(2-x)}$ is healed by the stripped off oxygen from CH_3CHO*-d in analogy to the Mars and van Krevelen mechanism [53].

In the absence of this healing process, the RuO_2(110) surface would continuously reduce further and eventually form metallic Ru islands on the surface under hydrogen rich and high temperature conditions [54]. However, the oxidizing potential of CH_3CHO can regenerate the bridging O^{br} atoms and counteracts the surface reduction. Subsequent to αC-O bond scission (reaction O6 in Table 1), the HDO pathway proceeds with ßC-H scission of CH_3CH* (reaction O7 in Table 1) as shown in Fig. 4(c). The calculated ΔE and E_a are -0.43 eV and 0.52 eV, respectively. At the TS, the bond lengths are 1.282 Å (ßC–H) and 1.407 Å (H*–O^{br}). The

regenerated O^{br} site in the previous step facilitates the ßC-H bond scission in CH_3CH^*. In that process, the C-C axis tilts towards the surface, a hydrogen atom from the methyl group of CH_3CH^* is exchanged with the O^{br} site, and the bridging hydroxyl is formed again. This is followed by hydrogenation of vinyl (CH_2CH^*) as shown in Fig. 4(d) via the reaction with the hydrogen atom from the neighboring bridging hydroxyl, which was formed in the previous ßC-H bond breaking step in CH_3CH^* (reaction O8 in Table 1). This reaction produces the final product CH_2CH_2. At the TS, $d_{O\text{-}H^*}$ is elongated to 1.346 Å. Once the hydrogen forms a bond with the αC of CH_2CH^*, the formed CH_2CH_2 spontaneously desorbs from the surface. The calculated E_a and ΔE are 0.85 eV and 0.15 eV, respectively.

An alternative hydrogenation pathway for the CH_2CH^* intermediate exists, which requires the adsorption of an additional hydrogen molecule similar to the vacancy creation mechanism described above (reaction O9 in Table 1). Upon adsorption, the H_2 molecule spontaneously dissociates and forms a hydroxyl species on a three-fold coordinated surface oxygen atom (O^{3f}) and the second H atom binds to the existing bridging hydroxyl, leading to an adsorbed H_2O^* species. The ΔE of this dissociative adsorption is exothermic by -0.30 eV. The $O\text{-}H^{3f}*$ can now act as a hydrogen donor to form CH_2CH_2 as shown in Fig. 4(e). The calculated ΔE and E_a are -0.32 eV and 0.82 eV, respectively. Similar to CH_2CH_2 production in the absence of an additional H_2 molecule (reaction O8), CH_2CH_2 desorbs from the surface as soon as it is formed. Spontaneous H_2O^* formation in reaction O9 is quite interesting because it allows for a very facile H_2O^* formation mechanism and vacancy regeneration with a lower E_a than is required for the initial vacancy formation process (reactions O1 to O3 in Table 1). In other words, once the initial vacancy on the RuO_2(110) surface has been created, the surface can be repeatedly oxidized and reduced during the HDO cycle and a separate site regeneration step is not necessary.

Our proposed HDO mechanism on RuO_2(110) shows similarities but also differences to a recently published HDO mechanism of CH_3CHO on the MoO_3(010) surface by Mei. *et al* [52]. In good agreement with our mechanism, CH_3CHO adsorbs on a MoO_3 vacancy site with two

different adsorption configurations (CH_3CHO*-s and CH_3CHO*-d) that are similar to CH_3CHO on RuO_2. However, on the MoO_3(010) surface the more plausible HDO pathway is only initiated from CH_3CHO*-s rather than CH_3CHO*-d as we have shown on RuO_2(110). The CH_3CHO*-d on MoO_3 leads to CH_3* and CO* with a large energy barrier (1.43 eV), after αC-H bond breaking in CH_3CHO*-d. In contrast, both CH_3CHO*-s and CH_3CHO*-d species on RuO_2 lead to αC-O bond scission in the subsequent step. The largest reaction barrier along the HDO pathway on RuO_2 is E_a = 0.83 eV (or E_a = 0.93 eV, if the initial vacancy formation step is considered), while on the MoO_3 surface a barrier of 1.39 eV needs to be overcome. These results suggest that RuO_2 catalysts show a better selectivity and higher activity than MoO_3.

After having carefully investigated 37 possible elementary steps for vacancy formation and HDO pathways over the RuO_2 catalyst, we summarize our results in the potential energy surface (PES) given in Fig. 5(a+b). Based on the thermodynamic phase diagram, we start with an equilibrated RuO_2 surface on which the majority of the bridging oxygen atoms are hydroxylated at the given reaction conditions [(2) in Fig. 5(a)]. After additional hydrogen adsorption and activation H_2O* forms on the bridging site of the RuO_2 surface. The desorption of H_2O* leaves an oxygen vacancy behind and forms the partially reduced $RuO_{(2-x)}$ surface, which is active for HDO [(6) in Fig. 5(a)]. CH_3CHO can adsorb on this vacancy site [(2) in Fig. 5(b)] and after the CH_3CHO*-s precursor state, isomerization leads to the more stable CH_3CHO*-d configuration, in which both αC and O are interacting with surface [(3) in Fig. 5(b)]. The next step is deoxygenation of CH_3CHO*-d to CH_3CH* via the desired αC-O bond scission step, which simultaneously re-oxidizes the $RuO_{(2-x)}$ surface and heals the vacancy [(4) in Fig. 5(b)]. The CH_3CH* intermediate adsorbed on the Ru^{cus} site is dehydrogenated by interaction with an empty bridging oxygen and decomposes into CH_2CH* [(5) in Fig. 5(b)]. The final part of the mechanism requires hydrogenation, which converts CH_2CH* to ethylene either by reacting with a three-fold hydroxyl resulting from dissociative adsorption of H_2 [(7) in Fig. 5(b)] or an already existing bridging hydroxyl [(9) in Fig. 5(b)]. Both mechanisms are feasible and probably occur

simultaneously, but the former has slightly better energetics and the significant advantage of regenerating the oxygen vacancy with a lower barrier than the latter mechanism. C-C bond breaking is unfavorable in all intermediates investigated and our results suggest a high selectivity towards the desired C-O bond scission pathway.

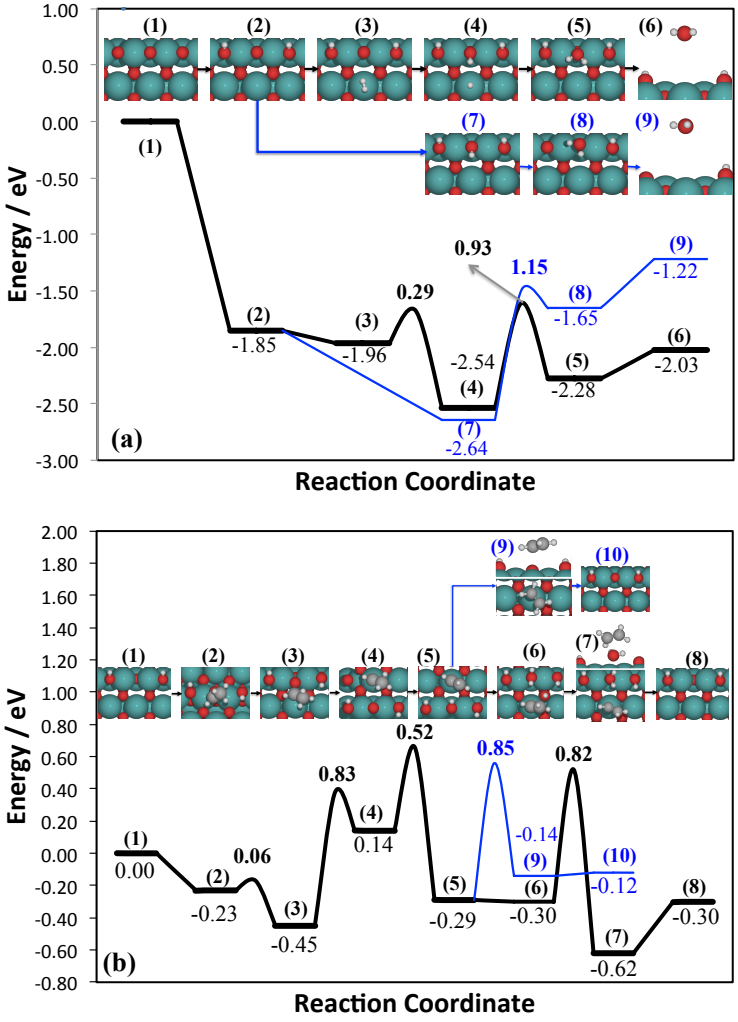

Fig. 5. Potential energy surface of (a) O-vacancy formation and (b) CH_3CHO HDO on the $RuO_{(2-x)}$(110) surface (white – hydrogen / red – oxygen / gray – carbon / teal – ruthenium). The black and blue numbers indicate the binding energy (E_{BE}) and activation energy (E_a), respectively. The solid black and blue lines represent the most preferred reaction pathway of CH_3CHO HDO and competitive reaction pathway for $CH_2CH_{2(g)}$ formation, respectively. (a) Intermediate states during O-vacancy formation: (1) RuO_2, stoichiometric surface; (2) O-2Hbr*; (3) O-2H^{br}* + Ru-H$_2$^{cus}*, H_2 adsorption on Ru^{cus}; (4) O-3H^{br}* + Ru-Hcus*; (5) O-2H^{br}* + H$_2$O^{br}*; (6) $RuO_{(2-x)}$ + $H_2O_{(g)}$, (7) O-3H^{br}*; (8) O-H^{br}* + H$_2$O^{br}*; (9) $RuO_{(2-x)}$ + $H_2O_{(g)}$; (10) (b) Intermediate states during CH_3CHO HDO: (1) $RuO_{(2-x)}$; (2) CH_3CHO*-s; (3) CH_3CHO*-d; (4) Ru-CH_3CH^{cus}*; (5) Ru-CH_2CH^{cus}*; (6) Ru-CH_2CH^{cus}* + O-H^{3f}*; (7) $CH_2CH_{2(g)}$; (8) $RuO_{(2-x)}$; (9) $CH_2CH_{2(g)}$; (10) RuO_2-2H^{br}*.

3.2 HDO of CH_3COH on Ru(0001)

After discussing HDO in detail on Ru-oxide, we will now focus on the HDO mechanism of CH_3CHO on Ru(0001) and compare the mechanisms on both surfaces. Following the same approach as for RuO_2(110), we only present key elementary steps in Table 2 due to the large number of 33 steps investigated. The adsorption configurations of intermediates involved in the key elementary steps are summarized and shown in Fig. 6 (a~j). Due to the complex adsorption geometries of the intermediates commonly used standard adsorption site naming, *i.e.* top, bridge, 3-fold, etc., do not allow for a detailed enough description. Hence, we augment the notation by using the terminology, $\mu^i\eta^j$, where 'i' and 'j' indicate the number of atoms interacting between adsorbates (i) and the surface (j), respectively.

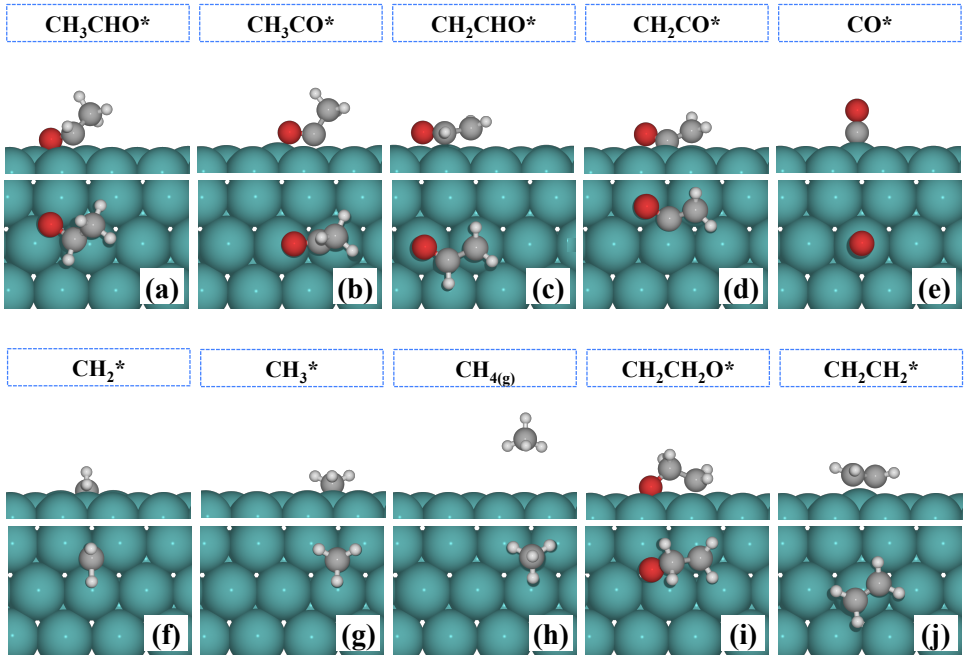

Fig. 6. Most stable adsorption configurations of selected intermediates during CH_3CHO HDO on Ru(0001) (white – hydrogen / red – oxygen / gray – carbon / teal – ruthenium). Atomic species (H, O, and C) are not included. (a) CH_3CHO*; (b) CH_3CO*; (c) CH_2CHO*; (d) CH_2CO*; (e) CO*; (f) CH_2*; (g) CH_3*; (h) $CH_{4(g)}$; (i) CH_2CH_2O*; (j) CH_2CH_2*.

The Ru(0001) metal surface has four different high-symmetry adsorption sites (top, bridge, hcp, and fcc). Iker del Rosal *et al.* have reported a total of seven different adsorption sites including three additional sites (two tetrahedral and octahedral), which are not considered in our study, because these sites are reported energetically unfavorable for high coverage of hydrogen

[55]. CH_3CHO can adsorb on the Ru(0001) surface in multiple configurations and we identified $\mu^2\eta^3$ adsorption as the most stable adsorption geometry with E_{BE} = -0.09 eV shown in Fig. 6(a). In this configuration the oxygen and αC atom of CH_3CHO binds at the bridge and top site, respectively. The C=O axis of CH_3CHO is nearly parallel to the surface, indicating that π-bonding of the C=O orbitals and the lone pair electrons of oxygen are interacting with the d-band electrons of the Ru surface atoms [56, 57].

Table 2. List of elementary steps of HDO in the main reaction pathway for CH_3CHO HDO on the Ru(0001) surface.

no.	Reaction	E_{int}^{IS}	E_{int}^{FS}	E_a	ΔE	ν
M0	$H_2 + 2* \rightarrow 2H*$	.	.	.	-0.76	.
M1	$CO_{(g)} + * \rightarrow CO*$	.	.	.	-1.52	.
M2	$CH_3CHO_{(g)} + * \rightarrow CH_3CHO*$	.	.	.	-0.09	.
M3	$CH_2CH_{2(g)} + * \rightarrow CH_2CH_2*$	.	.	.	-0.77	.
M4	$CH_3CHO* \rightarrow CH_3CO* + H*$	0.00	0.26	0.20	-0.84	352.9i
M5	$CH_3CHO* \rightarrow CH_2CHO* + H*$	0.00	0.27	0.46	-0.47	84.9i
M6	$CH_2CHO* \rightarrow CH_2CO* + H*$	0.00	0.17	0.31	-0.38	788.8i
M7	$CH_3CO* \rightarrow CH_2CO* + H*$	0.00	0.43	0.84	-0.02	868.1i
M8	$CH_2CO* \rightarrow CH_2 * + CO*$	0.45	0.41	0.52	-0.69	141.2i
M9	$CH_2* + H* \rightarrow CH_3*$	0.27	0.00	0.75	0.26	845.8i
M10	$CH_3* + H* \rightarrow CH_{4(g)}$	0.32	0.00	1.11	-0.13	942.5i
M11	$CH_2* \rightarrow CH* + H*$	0.00	0.28	0.12	-0.62	854.4i
M12	$CH* \rightarrow C* + H*$	0.00	0.23	1.00	0.08	854.4i
M13	$CH_2CHO* + H* \rightarrow CH_2CH_2O*$	0.32	0.22	1.16	0.66	638.8i
M14	$CH_2CH_2O* \rightarrow CH_2CH_2* + O*$	-0.05	0.52	0.50	-0.96	471.8i
M15	$CH_2CH_2* \rightarrow CH_2CH_{2(g)}$	0.00	0.00	0.54	0.47	80.1i
M16	$H* + O* \rightarrow OH*$	0.41	0.04	1.77	0.80	1371.1i
M17	$H* + OH* \rightarrow H_2O_{(g)}$	0.65	0.00	1.70	0.39	1124.3i
M18	$O* + CO* \rightarrow CO_2*$	0.19	0.00	1.77	1.43	443.5i

- E_{int}^{IS}, E_{int}^{FS}, E_a, and ΔE are in eV.
- E_{int} denotes the interactions between adsorbates in the IS and FS during NEB calculations.
- ν denotes the frequency of the imaginary mode at the transition state in cm^{-1}.
- ΔE and E_a are the total energy change and activation energy barriers without ZPE correction.

After molecular adsorption of CH_3CHO on the Ru surface the calculated $d_{C=O}$ and d_{C-C} of CH_3CHO are elongated by 16 % to 1.421 Å and by 0.79 % to 1.523 Å with respect to the gas-phase molecule, respectively. This results is consistent with adsorption of CH_3CHO on Mo(110) [58], Pt(111) [57], Pd(110/111) [59], and Rh(111) [60] where CH_3CHO adsorbs in both $\mu^1\eta^1$ and

$\mu^2\eta^3$ configurations at low temperature primarily through interaction of the oxygen atom and the surface. The $\mu^1\eta^1$ adsorption configuration is only stable at low temperatures and as the temperature increases, only the more stable $\mu^2\eta^3$ configuration remains on the surface. These results are further supported by extended Hückel calculations [61] that also predict the $\mu^2\eta^3$ configuration to be more stable than the $\mu^1\eta^1$ geometry.

As on RuO_2 adsorbed CH_3CHO^* has four decomposition pathways involving the previously discussed distinct bond breaking steps. However, important differences between the energetic results on both surfaces exist. The kinetically and thermodynamically preferred initiation of possible HDO pathways are the two αC-H and ßC-H bond breaking steps (reaction M4 and M5 in Table 2). Reaction M4 is the αC-H scission in CH_3CHO^* leading to CH_3CO^* with E_a = 0.20 eV and ΔE = -0.84 eV depicted in Fig. 7(a). At the TS, $d_{C\text{-}H}$ is elongated to 1.143 Å, and the elongated hydrogen is pointing towards the fcc site. Following the reaction coordinate further, the H atom diffuses to the hcp site due to repulsion between hydrogen and the acetyl (CH_3CO^* - $\mu^3\eta$) intermediate. Reaction M5 refers to the ßC-H bond breaking step in CH_3CHO^* producing adsorbed CH_2CHO^* with E_a = 0.46 eV and ΔE = -0.47 eV. Although the activation barrier of reaction M5 is a slightly higher than that of reaction M4, reaction M5 must be considered feasible at practical HDO reaction temperatures and we consider reaction M4 and M5 as competitive pathways. The adsorption configurations of the two resulting intermediates, CH_3CO^* ($\mu^2\eta^2$) and CH_2CHO^*($\mu^6\eta^3$) are shown in Fig. 6(b) and (c).

The CH_2CHO^* intermediate can further decompose along four different pathways to form CH_2^* + COH* (M28), CHCHO* + H* (M30), CH_2CH^* + O* (M29), and CH_2CO^* + H*(M6 in Table 2). Reaction M6 leading to CH_2CO^* and H* is the kinetically preferred pathway with E_a = 0.31 eV and ΔE = -0.38 eV. The other possibilities have significantly higher barriers as listed in Table S2 in the Appendix). The alternative first decomposition product of CH_3CHO^* is CH_3CO^*, which can also be dehydrogenated to CH_2CO^* via reaction M7 in Table 2 (shown in Fig. 7(b)). At the TS, the C-C axis tilts towards the Ru surface to facilitate ßC-H bond activation, and $d_{C\text{-}H}$ is

elongated to 1.155 Å as shown in Fig. 7(b). This reaction is quasi thermoneutral (ΔE = -0.02) and the calculated E_a is 0.84 eV. Although the exact order of the first two C-H bond activation steps cannot be conclusively determined on the basis of our results alone, we note that both reactions M6 and M7 lead to same ketene [CH_2CO^* / Fig. 6(d) - $\mu^3\eta^3$] intermediate. At this point of the mechanism, the C-C bond of CH_2CO^* is easily broken in a decarbonylation reaction to form carbon monoxide (CO*) and methylene (CH_2^*) via step M8 (E_a = 0.52 eV and ΔE = -0.69 eV). The carbon monoxide (CO*) fragment of CH_2CO^* is strongly adsorbed through its carbon atom on top of the Ru [E_{BE} = -1.52 eV / Fig. 6(e) - $\mu^1\eta^1$], in good agreement with other theoretical and experimental data [62, 63]. The CH_2^* fragment, however, is unfavorably bound to the hcp site [E_{BE} = 1.12 eV / Fig. 6(f) - $\mu^3\eta^3$] with respect to CH_4 and H_2 in the gas phase, which also agrees well with previous results [64].

The intermediate CH_2^* can proceed either through a hydrogenation or dehydrogenation pathway, which depends on the reaction conditions. The former hydrogenation pathway leads to methane (CH_4) in the gas phase, while the latter dehydrogenation pathway results in carbon deposition on the surface (coking). Before we discuss the hydrogenation process occurring via reaction M9 and reaction M10 in Table 2 in detail, we note that the binding preference of hydrogen in the presence of co-adsorbed CH_2^* and CH_3^* is altered. On the clean Ru(0001) surface H atoms adsorb on fcc sites with E_{BE} = -0.61 eV, but when CH_2^* and CH_3^* are co-adsorbed, the hcp site is found to be the most favorable adsorption site. These adsorption site preferences are in good agreement with other DFT and experimental data [64]. The adsorbed CH_2^* ($\mu^2\eta^3$, E_{BE} = 1.17 eV) can then be hydrogenated with a H* atom from the hcp site to methyl (CH_3^*, $\mu^4\eta^3$, E_{BE} = 0.77 eV) and the corresponding energetics are E_a = 0.75 eV and ΔE = 0.26 eV (Figure 5(d)). The resulting CH_3^* intermediate can be further hydrogenated to CH_4 through reaction M10 with E_a = 1.11 eV and ΔE = -0.13 eV as shown in Fig. 7(e). At the TS, $d_{C\text{-}H}$ is 1.614 Å in case of the reaction M9 and 1.556 Å in case of the reaction M10. The second hydrogenation of CH_3^* to CH_4 has a higher activation barrier than the first hydrogenation of CH_2^*, which is

consistent with other DFT studies of the methanation reaction over various model catalyst surfaces [65, 66].

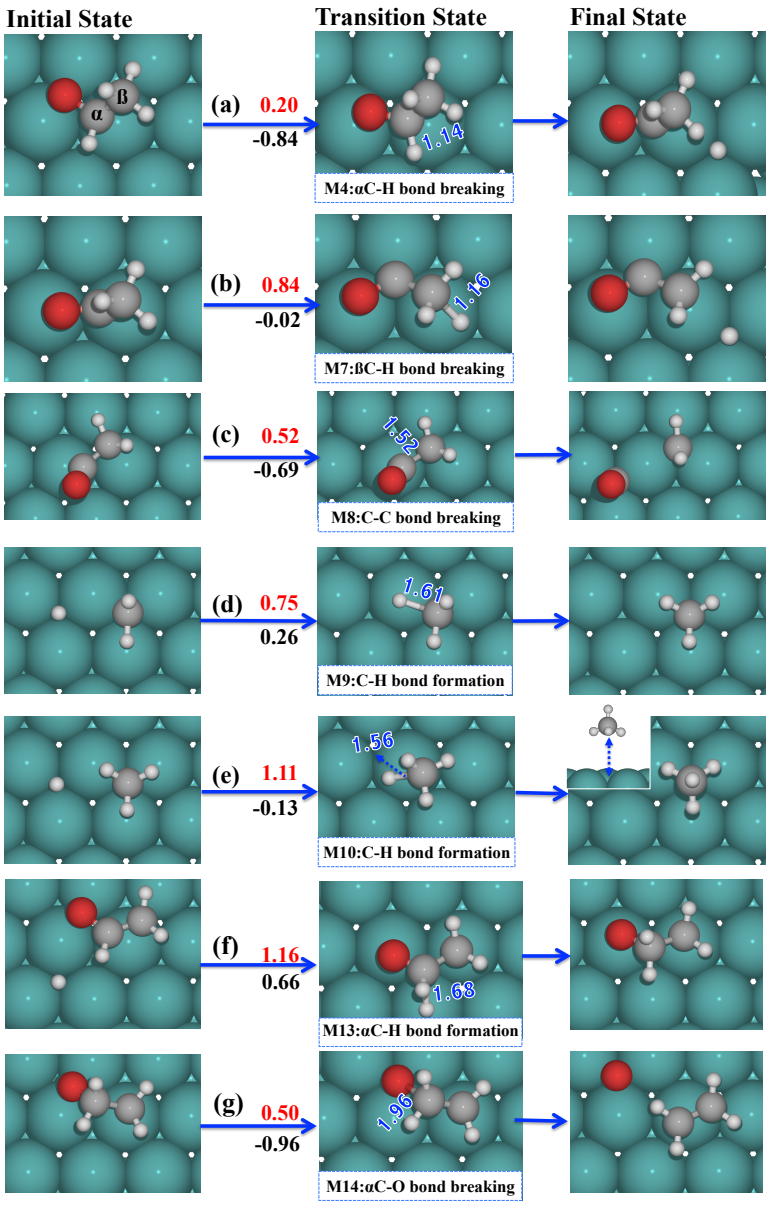

Fig. 7. Calculated reaction pathway of CH_3CHO HDO on Ru(0001) (white – hydrogen / red – oxygen / gray – carbon / teal – ruthenium). Numerical values in red, black and blue represent the activation energy barrier E_a [eV], the reaction energy ΔE [eV] and bond distance [Å], respectively. (a) Reaction M4: $CH_3CHO^* \rightarrow CH_3CO^* + H^*$, (b) Reaction M7: $CH_3CO^* \rightarrow CH_2CO^* + H^*$, (c) Reaction M8: $CH_2CO^* \rightarrow CH_2^* + CO^*$, (d) Reaction M9: $CH_2^* + H^* \rightarrow CH_3^*$; (e) Reaction M10: $CH_3^* + H^* \rightarrow CH_{4(g)}$; (f) Reaction M13: $CH_2CHO^* + H^* \rightarrow CH_2CH_2O^*$; (g) Reaction M14: $CH_2CH_2O^* \rightarrow CH_2CH_2^* + O^*$.

Along the hydrogenation coordinate ($C^* + 4H^* \rightarrow CH^* + 3H^* \rightarrow CH_2^* + 2H^* \rightarrow CH_3^* + H^* \rightarrow CH_4$), the total energy of the TS keeps increasing, suggesting that the last CH_3^*

hydrogenation is the rate-determining step (RDS), which also is associated with the highest individual reaction barrier in this reaction sequence [66]. Once the CH_3* forms a bond with the surface hydrogen, the formed CH_4 desorbs spontaneously from the surface. Alternatively, the CH_2* intermediate can also be dehydrogenated to methylidyne (CH*) and H* (reaction M11) followed by CH* decomposition into C* and H* (reaction M12) on the surface. In both reactions, the separated hydrogen atom moves to the fcc site, while the CH_2* and CH* species stay at the hcp site during the reactions. The calculated E_a and ΔE are 0.12 eV and -0.63 eV for reaction M11 and 1.00 eV and 0.08 eV for reaction M12, respectively. From a thermodynamic and kinetic perspective the dehydrogenation of CH_2* to surface carbon is preferred over the hydrogenation pathway to CH_4. Hence, carbon deposition on Ru surface is expected, which can eventually lead to catalyst deactivation. These predictions are in agreement with a study by Cheng *et al.*, reporting that among Re, Fe, Co, Rh and Ru, Ru catalysts are the least suited catalysts for methanation because of a high effective energy activation barrier for CH_4 formation [65]. On the other hand, the same study reports that Ru is the best catalyst for C-C coupling reactions and if we invoke the concept of microscopic reversibility this further suggests that C-C bond scission is also effectively catalyzed.

The low energy reaction pathways of CH_3CHO on Ru(0001) discussed so far are unselective towards C-O bond breaking required for HDO and coke deposition or, in the most optimistic scenario, decarbonylation to methane takes place. The desired product CH_2CH_2, which is preferentially produced on RuO_2(110), is unlikely to be formed on metallic Ru, but one of the powerful advantages of computational catalysis tools is the possibility to investigate the mechanism even of unselective pathways. The mechanism leading to CH_2CH_2 formation starts from adsorbed CH_2CHO* ($\mu^6\eta^3$) and the necessary steps are shown in Fig. 7(f) and (g). Hydrogenation at the ßC through reaction M13 forms CH_2CH_2O* [$\mu^2\eta^3$, E_{BE} = 0.09 eV] displayed in Fig. 6(i). The calculated E_a and ΔE are 1.16 eV and 0.66 eV, respectively, and the $d_{C\text{-}H}$ distance at the TS is 1.678 Å. The resulting CH_2CH_2O* intermediate is then deoxygenated through step

M14 as shown in Fig. 7(g). The dissociated oxygen moves to hcp site in the FS and CH_2CH_2* ($\mu^2\eta^1$) preferentially adsorbs on the top site with E_{BE} of -0.77 eV. At the TS, $d_{C\text{-}O}$ is elongated from 1.457 Å to 1.963 Å. The E_{BE} of formed CH_2CH_2* and oxygen is exothermic by -0.87 eV with respect to the energy of H_2O and CH_3CHO gas phase. Contrary to RuO_2(110), the formed CH_2CH_2* does not spontaneously desorb from the surface, but stays adsorbed on top of the Ru atom. This configuration of CH_2CH_2 adsorption is well consistent with previous DFT calculations [56]. The desorption step has an activation barrier E_a = 0.54 eV and is endothermic with ΔE =0.47 eV.

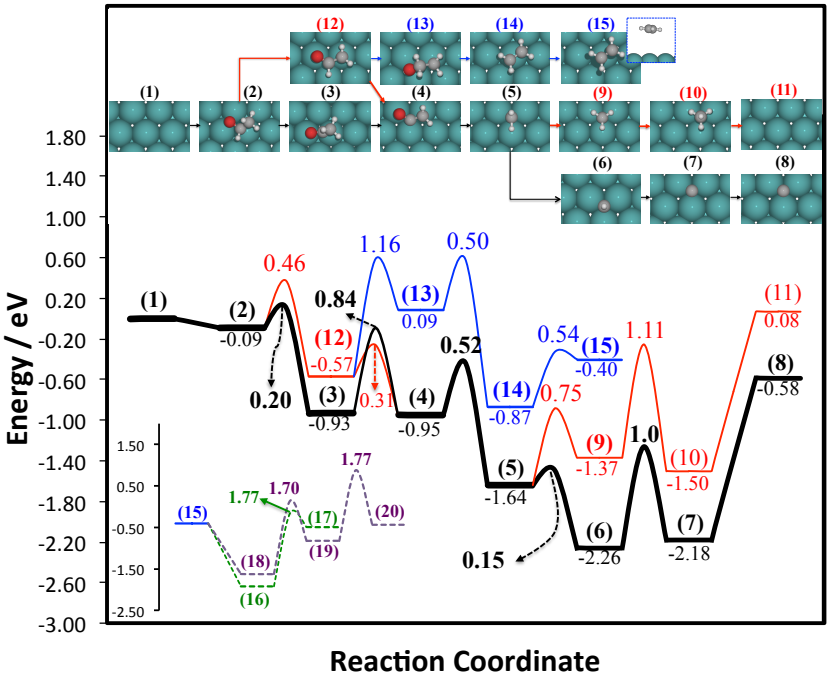

Fig. 8. Potential energy surface of CH_3CHO HDO on Ru(0001) surface (white – hydrogen / red – oxygen / gray – carbon / teal – ruthenium). The black and blue numbers indicate the binding energy (E_{BE}) and activation energy (E_a), respectively. The solid black, blue, and red lines represent the most preferred pathway, $CH_2CH_{2(g)}$ formation, and $CH_{4(g)}$ formation, respectively. The green and purple dotted lines represent O* removal from Ru(0001) surface. Intermediate states are (1) Ru (clean surface); (2) CH_3CHO*; (3) CH_3CO* + H*; (4) CH_2CO* + 2H*; (5) CH_2* + CO* + 2H*; (6) CH* + CO* + 3H*; (7) C* + CO* + 4H*; (8) C* + 4H*(after CO desorption); (9) CH_3* + CO* + H*; (10) $CH_{4(g)}$ + CO*; (11) Ru (clean surface after CO desorption); (12) CH_2CHO* + H*; (13) CH_2CH_2O*; (14) CH_2CH_2* + O*; (15) $CH_2CH_{2(g)}$ + O*; (16) O* + CO* (CO adsorption); (17) CO_2*; (18) O* + 2H* (dissociative H_2 adsorption); (19) OH* + H*; (20) H_2O*.

A summary of the elementary steps leading to surface carbon, CH_4 and CO, and CH_2CH_2 starting from CH_3CHO on Ru(0001) are summarized in form of a PES in Fig. 8. The CH_3CHO

molecule adsorbs on Ru through the C=O group [(2) in Fig. 8] and then proceeds through two competitive dehydrogenation pathways [αC-H (3) / ßC-H (9) in Fig. 8] leading to the same intermediate, CH_2CO* [(4) in Fig. 8]. This is followed by C-C bond breaking resulting in CO* and CH_2* [(5) in Fig. 8]. The intermediate, CH_2*, can be either successively hydrogenated to CH_4 [(5) → (6) in Fig. 8] or even more readily dehydrogenated to surface carbon [(5) → (6) in Fig. 8]. The unselective HDO pathway is also included and branches from the main pathway at the CH_2CHO* intermediate. It can be hydrogenated to CH_2CH_2O* [(10) in Fig. 8] with a relatively high barrier E_a = 1.16 eV, which is then deoxygenated to CH_2CH_2* on the surface [(11) in Fig. 8]. The chemisorbed CH_2CH_2* eventually desorbs from the surface into the gas phase with a barrier of E_a = 0.54 eV. Lastly, the oxygen atom that remains on the Ru(0001) surface must also be removed in order to close the catalytic cycle. For this, we have considered stepwise hydrogenation to H_2O and the reaction with CO* to CO_2. Both pathways have large barriers of ca. 1.8 eV, which is significantly higher than the barriers for the steps required for CH_2CH_2 formation. Hence, the removal of O* from Ru(0001) is the slowest step and unless the temperatures are high enough to overcome the barrier for H_2O or CO_2 formation, the surface will slowly accumulate chemisorbed oxygen and may evolve into a surface oxide.

In our above analysis we assumed CO to be a reaction product that desorbs after its formation or it scavenges surface O* to produce CO_2. However, Ru is not only known to be an active catalyst for CO oxidation [25, 67], but also for Fischer-Tropsch (FT) synthesis [63, 68, 69], which may lead to CH_4 and higher alkanes through syngas reactions. Because of its general catalytic importance, adsorption and dissociation of CO on Ru(0001) have been extensively studied. According to the CO adsorption and dissociation study on Ru(0001) surface at elevated pressures [63], the saturation CO coverage is ca. 0.66 ML under UHV conditions and adsorbed CO* on top is stable up to 450 K. Upon temperature increase to 485 K the CO coverage decreases to 0.58 ML, indicating molecular CO desorption from the surface. At higher temperatures (> 520 K), a significant amount of carbon deposits on the surface is observed and attributed to CO

dissociation. A sizeable number of studies report that during FT synthesis hydrocarbons (C_xH_y) or even polymeric chains could be formed via the carbide mechanism over the Co, Fe, and Ru catalysts [65, 70]. However, recent DFT calculations on Co and Ru catalysts have shown that there are non-dissociative FT pathways that involve carbon-carbon coupling, rather than the carbide mechanism [69]. Regardless of the still debated details of the FT mechanism, we note here that CO can be further hydrogenated at practical HDO conditions with high partial pressures of H_2. As a result, CO may be converted to either liquid hydrocarbons or methane as suggested by Paraskevi *et al.* and Ciobîcă *et al.* [62, 64]. While these open questions are certainly relevant for a complete process design, we will not attempt to address these issues in our present work and keep our focus on understanding reaction pathways on metal and metal-oxide catalyst surfaces that preferentially break C-O bonds rather than C-C bonds.

3.3 Comparison of CH_3CHO HDO on RuO_2(110) and Ru(0001)

In the case of RuO_2(110), HDO of CH_3CHO is initiated by formation of an oxygen vacancy, followed by αC-O bond breaking of CH_3CHO*-d, leaving the CH_3CH* intermediate and bridging hydroxyl on the surface. The relative feasibility of αC-O bond breaking (E_a = 0.83 eV) over C-C bond breaking (E_a = 1.46 eV) can be rationalized by a simple analysis of the adsorbate bond lengths: the longer the bond distance, the weaker the bond strength. Along the HDO reaction of CH_3CHO from the gas phase molecule to the bidentate configuration, the C=O bond length in CH_3CHO is steadily increasing (gas phase= 1.224 Å → CH_3CHO*-s= 1.277 Å → CH_3CHO*-d= 1.392Å), whereas the C-C bond length is approximately constant (gas phase= 1.511 Å → CH_3CHO*-s= 1.494 Å → CH_3CHO*-d= 1.520 Å). Hence, we could simply conclude that C-O bond scission becomes more feasible than C-C bond scission as the reaction is moving toward the bidentate configuration. The bond weakening can also be explained on the basis of electronic structure arguments. Hybridization of αC with the Ru^{cus} site leads to charge transfer from αC to the Ru^{cus} site. This is counteracted by electron back-donation to the anti-bonding σ* orbital of

C=O, which strengthens the adsorbate coupling with the substrate while at the same time the C=O bond is weakened [47]. The CH_3CH^* intermediate is then successively de/hydrogenated to CH_2CH_2 (see the PES in Fig. 5). The largest activation barrier in the overall reaction is encountered for the 2nd hydrogen transfer during the initial vacancy formation (E_a = 0.93 eV, reaction O3 in Table 1), but this step may be avoided under steady-state reaction conditions because the vacancy can be regenerated during the HDO reaction with additional hydrogen molecular adsorption. Depending on which vacancy formation mechanism dominates, the RDS of CH_3CHO HDO on RuO_2(110) is either the initial vacancy formation or the hydrogenation of CH_2CH^* to CH_2CH_2 (E_a = 0.82 eV, reaction O10). The overall reaction is then given by

$$CH_3CHO_{(g)} + H_{2(g)} \rightarrow CH_2CH_{2(g)} + H_2O_{(g)} \quad [\Delta E = -0.30 \text{ eV}]. \tag{26}$$

Whereas HDO is selectively catalyzed on RuO_2(110), Ru(0001) is more likely to catalyze the DCN (decarbonylation) reaction. CH_3CHO adsorbs on the clean Ru surface in the $\mu^2\eta^3$ configuration and decomposes in two competing dehydrogenation steps into the CH_2CO^* intermediate. The C-C bond of CH_2CO^* is more easily activated (E_a = 0.52 eV) than the C-O bond (E_a = 1.44 eV) resulting in adsorbed CH_2^* and CO^* intermediates on surface. Sequential hydrogenation or dehydrogenation of the CH_2^* intermediate can lead to gas phase CH_4 production or carbon deposition and catalyst deactivation. The more energetically favorable reaction, however, is dehydrogenation and coke formation, given by the following reaction equation

$$CH_3CHO_{(g)} \rightarrow C^* + 2H_{2(g)} + CO_{(g)} \quad [\Delta E = 1.87 \text{ eV}]. \tag{27}$$

This overall reaction is endothermic by +1.87 eV under the assumption of CO and H_2 desorption. The most activated step with E_a = 1.00 eV is the dehydrogenation of CH^* (reaction M12). If instead CH_4 is formed as a reaction product the largest activation barrier E_a = 1.11 eV occurs for the final CH_3^* hydrogenation to CH_4. The overall reaction is given by

$$CH_3CHO_{(g)} \rightarrow CH_{4(g)} + CO_{(g)} \quad [\Delta E = 0.08 \text{ eV}]. \tag{28}$$

If we consider the nonselective HDO pathway over Ru as given by the equation $CH_3CHO_{(g)} + H_{2(g)} \rightarrow CH_2CH_{2(g)} + H_2O_{(g)}$, the most difficult step is the removal of surface oxygen as H_2O (step M16 and M17) or CO_2 (M18). Both pathways require surmounting energy barriers of ca. 1.8 eV, which indicates the strong oxygen affinity of metallic Ru and its tendency to accumulate oxygen causing high oxygen coverage or even the formation of a surface oxide layer. In fact, it is experimentally well known that Ru can be easily oxidized and reduced depending on its environment and the oxidation state of the surface under working conditions depends on the rates of oxygen delivery and removal to and from the surface [25, 46, 71, 72]. These results clearly indicate that ethylene formation is much less likely on Ru(0001) than carbon deposition or methane formation.

In conclusion, the HDO reaction pathways on the $RuO_2(110)$ surface favors the ideal HDO pathway that produces selectively CH_2CH_2, while the reaction network on the Ru(0001) metal surface shows complex reaction pathways that preferentially lead to decarbonylation (DCN) and the generation of CH_4 or more favorably carbon deposits.

3.4 HDO of CH_3COH on $RuO_2/TiO_2(110)$

$RuO_2(110)$ can selectively convert CH_3CHO to CH_2CH_2 with a moderate energy barrier. However, it is well known that RuO_2 catalysts tends to form volatile oxides at higher temperature and form metallic-Ru islands under highly reducible conditions, which restrict its use for high-temperature and high H_2 pressure applications. Many efforts have been applied to increase the stability of RuO_2 by changing the dominant rutile structure to a perovskite-type structure [73, 74]. This structure, however, suffers from low catalytic activity due to decreased surface area. Another idea is to mix RuO_2 with TiO_2, because TiO_2 is more stable under strong reducing conditions, and has the same rutile structure and a similar lattice constant as RuO_2. We propose here a catalyst model system that is based on TiO_2, but the Ti atoms in the topmost layer are substituted with Ru atoms ($RuO_2/TiO_2(110)$) as shown in Fig. 9. We anticipate that the catalytic surface properties are

similar to the ones obtained for RuO_2, while the TiO_2 support may stabilize the Ru atoms in the positions of the rutile phase and reduce the reduction tendency of RuO_2. Indeed, our calculated surface phase diagram (see Appendix S. 15) shows that $RuO_2/TiO_2(110)$ is still partially reducible under HDO conditions, but shows much higher stability against high temperature and pressure conditions.

Oxygen vacancy formation and HDO pathways over the RuO_2/TiO_2 overlayer catalysts are summarized in the PES given as Fig. 10(a+b) and the calculated values of E_a and ΔE are tabulated in Table 3. Similar to the $RuO_2(110)$ surface, the $RuO_2/TiO_2(110)$ also shows the partially hydroxylated surface under practical HDO conditions. Based on the $RuO_2(110)$ results, we tested two vacancy formation pathways, namely the disproportionation (OT2 in Table 3) and consecutive hydrogenation pathway (OT3 and OT4 in Table 4). The calculated E_a and ΔE for disproportionation are 1.38 eV and 0.90 eV, respectively. The consecutive hydrogenation steps have the barriers and energy changes E_a = 0.47 eV / 1.26 eV and ΔE = -0.69 eV / 0.69 eV (OT3 / OT4 in Table 3), respectively.

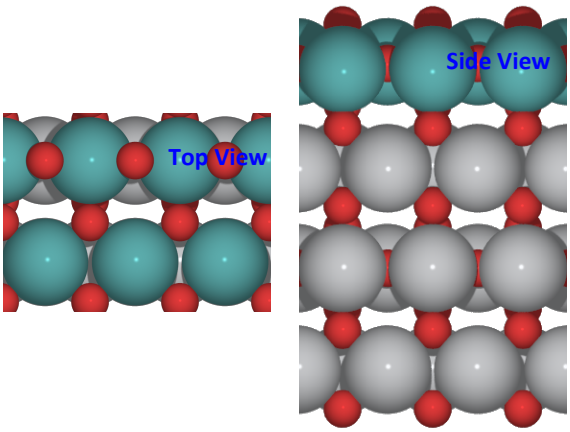

Fig. 9. Top (left) and side view (right) of stoichiometric $RuO_2/TiO_2(110)$ surface (red – oxygen / gray – titanium / teal – ruthenium).

Both pathways have higher energy barriers on $RuO_2/TiO_2(110)$ than on the $RuO_2(110)$ surface, which implies that the surface vacancy creation on the RuO_2/TiO_2 surface is harder and the stability under highly reducible conditions is increased. The desorption of H_2O* leaves an oxygen

vacancy behind and forms the partially reduced $RuO_{(2-x)}/TiO_2$ surface with $\Delta E = 0.10$ eV. As in the case of RuO_2, the formed vacancy provides the active site for HDO of CH_3CHO [(6) in Fig. 10(a)] and CH_3CHO can adsorb on this vacancy site [(2) in Fig. 10(b)].

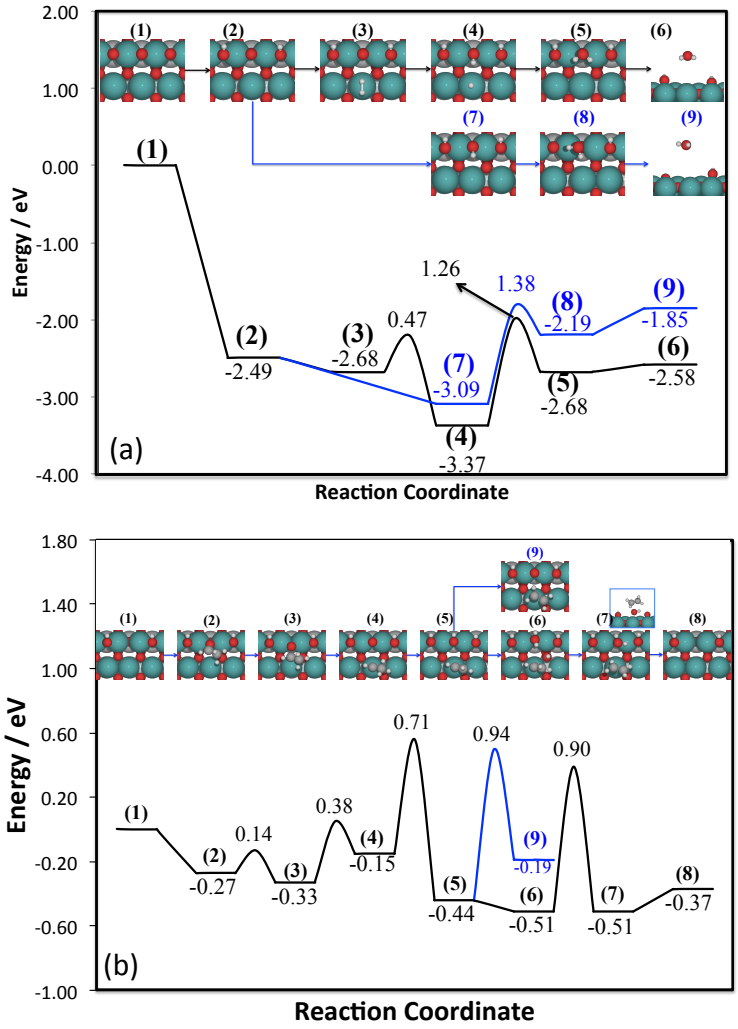

Fig. 10. Potential energy surface of (a) O-vacancy formation and (b) CH_3CHO HDO on the $RuO_{(2-x)}/TiO_2(110)$ surface (white – hydrogen / red – oxygen / gray – carbon / teal – ruthenium). The black and blue numbers indicate the binding energy (E_{BE}) and activation energy (E_a), respectively. The solid black and blue lines represent the most preferred reaction pathway of CH_3CHO HDO and competitive reaction pathway for $CH_2CH_{2(g)}$ formation, respectively. (a) Intermediate states during O-vacancy formation: (1) RuO_2, stoichiometric surface; (2) O-$2H^{br}$*; (3) O-$2H^{br}$* + Ru-H_2^{cus}*, H_2 adsorption on Ru^{cus}; (4) O-$3H^{br}$* + Ru-H^{cus}*; (5) O-$2H^{br}$* + H_2O^{br}*; (6) $RuO_{(2-x)}$ + $H_2O_{(g)}$, (7) O-$3H^{br}$*; (8) O-H^{br}* + H_2O^{br}*; (9) $RuO_{(2-x)}$ + $H_2O_{(g)}$; (b) Intermediate states during CH_3CHO HDO: (1) $RuO_{(2-x)}$; (2) CH_3CHO*-s; (3) CH_3CHO*-d; (4) Ru-CH_3CH^{cus}*; (5) Ru-CH_2CH^{cus}*; (6) Ru-CH_2CH^{cus}* + O-H^{3f}*; (7) $CH_2CH_{2(g)}$; (8) $RuO_{(2-x)}$; (9) $CH_2CH_{2(g)}$.

After the CH_3CHO*-s precursor state, isomerization leads from the precursor state to the more stable CH_3CHO*-d configuration [(3) in Fig. 10(b)]. The calculated E_a and ΔE for this isomerization (OT6) are 0.14 eV and -0.06 eV, respectively.

Table 3. List of elementary steps in the main reaction pathway for O-vacancy formation and HDO of CH_3CHO on the $RuO_2/TiO_2(110)$ surface.

no.	Reaction	E_{BE}^{IS}	E_{BE}^{FS}	E_a	ΔE	ν
OT1[a]	$H_{2(g)} + 2O^{br} \rightarrow O\text{-}2H^{br}*$	.	.	.	-2.49	.
OT2	$O\text{-}H^{br}* + O\text{-}H^{br}* \rightarrow H_2O^{br}* + O^{br}$	-3.09	-2.18	1.26	0.90	1071.8
OT3	$Ru\text{-}H_2^{cus}* + O^{br} \rightarrow Ru\text{-}H^{cus}* + O\text{-}H^{br}*$	-2.68	-3.37	0.47	-0.69	858.6
OT4[b]	$Ru\text{-}H^{cus}* + O\text{-}H^{br}* \rightarrow Ru^{cus} + H_2O^{br}*$	-3.37	-2.58	1.38	0.79	912.9
OT5[c]	$CH_3CHO_{(g)} \rightarrow CH_3CHO*$	.	.	.	-0.27	.
OT6	$CH_3CHO*\text{-}s \rightarrow CH_3CHO*\text{-}d$	-0.27	-0.33	0.14	-0.33	122.7
OT7	$CH_3CHO*\text{-}d + Ru^{cus} \rightarrow Ru\text{-}CH_3CH^{cus}* + O^{br}$	-0.33	-0.15	0.38	0.18	206.9
OT8	$Ru\text{-}CH_3CH^{cus}* + O^{br} \rightarrow Ru\text{-}CH_2CH^{cus}* + O\text{-}H^{br}*$	-0.15	-0.44	0.71	-0.29	1185
OT9[d]	$Ru\text{-}CH_2CH^{cus}* + O\text{-}H^{br}* \rightarrow CH_2CH_{2(g)} + O^{br}$	-0.44	-0.19	0.94	0.25	813.1
OT10	$H_{2(g)} + O^{3f} + O\text{-}H^{br}* \rightarrow O\text{-}H^{3f}* + H_2O^{br}*$	.	.	.	-0.07	.
OT11[e]	$Ru\text{-}CH_2CH^{cus}* + O\text{-}H^{3f}* \rightarrow Ru^{cus} + CH_2CH_{2(g)}$	-0.51	-0.51	0.90	0.00	1256.3
OT12	$H_2O^{br}* \rightarrow H_2O_{(g)}$	.	.	.	0.14	.

- E_{BE}^{IS}, E_{BE}^{FS}, E_a, and ΔE are in eV.
- E_{BE} is the binding energy of surface intermediates referenced to the $RuO_{(2-x)}/TiO_2(110)$ surface and the gas phase molecules (H_2, H_2O, CH_3CHO, and CH_4) except for O0, which is referenced to the stoichiometric $RuO_2/TiO_2(110)$ surface. Superscripts IS and FS are acronyms of initial and final state.
- ν denotes the frequency of the imaginary mode at the transition state in cm^{-1}.
- ΔE and E_a are the total energy change and activation energy barriers without ZPE correction.
- [a] OT0 is the dissociative H_2 adsorption on the stoichiometric $RuO_2/TiO_2(110)$ surface.
- [b] OT4 is the adsorption of CH_3CHO on the O-vacancy site.
- [c] OT5 is the isomerization of the CH_3CHO-s intermediate.
- [d] OT9 is H_2 adsorption.
- [e] OT11 is H_2O desorption at the end of catalytic cycle.

The next step is deoxygenation (OT7) of CH_3CHO*-d to CH_3CH* via the desired αC-O bond scission step, which simultaneously re-oxidizes the $RuO_{(2-x)}/TiO_2$ surface and heals the vacancy [(4) in Fig. 10(b)]. The calculated E_a and ΔE are 0.38 eV and 0.18 eV, respectively. Compared to αC-O bond breaking on the RuO_2 surface, the αC-O bond scission on the $RuO_{(2-x)}/TiO_2$ surface has a lower E_a (0.45 eV) and is less endothermic, which suggests that the RuO_2/TiO_2 is more active for αC-O bond scission. The CH_3CH* intermediate adsorbed on the Ru^{cus} site is dehydrogenated by interaction with an empty bridging oxygen and decomposes into CH_2CH* [(5) in Fig. 10(b), OT8] with E_a = 0.71 eV and ΔE = -0.29 eV. The hydrogenation to convert from CH_2CH* to CH_2CH_2 occur either by reacting with an already existing bridging hydroxyl [(9) in

Fig. 10(b), OT9] or a three-fold hydroxyl resulting from dissociative adsorption of H_2 [(7) in Fig. 10(b), OT11]. The calculated E_a and ΔE for the former hydrogenation are E_a = 0.90 eV and ΔE = 0.00 eV, and for the later hydrogenation are E_a = 0.94 eV and ΔE = 0.25 eV, respectively. Both mechanisms are feasible and probably occur simultaneously, but the later has slightly better energetics in terms of the significant advantage of regenerating the oxygen vacancy with lower energy barrier.

Chapter 4. Conclusions

We have investigated hydrodeoxygenation mechanisms of acetaldehyde (CH_3CHO), which was chosen as a surrogate molecule for the ca. 400 oxygenated compounds in bio-oil obtained from the (fast) pyrolysis of biomass, on the Ru(0001), RuO_2(110), and RuO_2/TiO_2(110) surfaces by using DFT calculations. The equilibrated RuO_2(110) and RuO_2/TiO_2 surface structures under practical HDO conditions (T = 600 K / p_{H_2} = 200 bar) are populated with bridging hydroxyls as obtained form a surface phase diagram as a function of the chemical potentials μ_{H_2} and μ_{H_2O}. Further reduction can occur upon additional hydrogen adsorption and leads to the generation of an active oxygen vacancy site on the surface.

Total reduction to metallic Ru cannot be excluded, since it was not considered within the thermodynamic framework for the generation of the surface phase diagram. The surface vacancy plays a key role for the adsorption of the CH_3CHO molecule and it can be selectively converted to $CH_2CH_{2(g)}$ on the RuO_2(110) and the RuO_2/TiO_2 surfaces following the sequence of elementary steps given by: adsorption (CH_3CHO-s*) → isomerization (CH_3CHO*-d) → αC-O bond breaking (CH_3CH*) → ßC-H bond breaking (CH_2CH*) → αC-H bond formation ($CH_2CH_{2(g)}$). In contrast, the metallic Ru(0001) surface is not suitable for HDO and preferentially catalyzes the DCN reaction along the pathway: adsorption (CH_3CHO**)** → αC-H bond breaking (CH_3CO*) → ßC-H bond breaking (CH_2CO*) → C-C bond breaking (CH_2*) → C-H bond breaking (CH*) → C-H bond breaking (C*). The final product is surface carbon, which indicates coking and eventually leads to catalyst deactivation. If HDO does occur on Ru(0001), then the removal of surface O* via the formation of H_2O or CO_2 is the limiting reaction step. The accumulation of O* on the surface can lead to high oxygen coverage, partial oxidation or even the formation of a surface oxide.

Overall, our results show that the oxide and not the metallic phase of Ru-based catalysts perform the desired HDO reaction with reasonably low barriers and high selectivity. However,

the challenge of identifying the exact oxidation state of the surface under *in-situ* conditions remains.

Chapter 5. Future Research

5.1 Application of kinetic Monte Carlo (kMC) simulations

Activation energies of HDO elementary steps and binding energies of intermediates have been calculated using the periodic DFT method. With just these data resulted from DFT calculations we can not calculate the reaction rate and the rate determining step (RDS), because of the gap between DFT calculations and practical chemical conditions (temperature, pressure, and concentration), i.e., the DFT data are obtained on the shortest length and time scale, whereas practical reaction and reactor design requires longer time and length scale than the atomic DFT data. Therefore, we need a tool to bridge this gap. Very frequently, micro-kinetic modeling is used to bridge the pressure gap, but this method relies on the mean-field assumption and fails to describe the correct surface kinetics when adsorbate-adsorbate interactions or local ordering is important and diffusion is slow.

Another approach gaining significant interest recently are first principle-based kinetic Monte Carlo (kMC) simulations. This method combines all elementary steps involved in the catalytic cycle within a stochastic framework in order to evaluate surface chemical kinetics [75]. Reuter et al. have applied first principle-based kMC simulations to CO oxidation on the RuO_2(110) surface under steady-state conditions and obtained results in very good agreement with experimental data [76]. Since we are interested in rutile surfaces (RuO_2 and RuO_2/TiO_2) that have uneven electronic configuration on their surface (O^{br}, O^{3f}, and Ru^{cus}) leading to slow diffusion, the application of the kMC method would provide the best approach for bridging this pressure gap.

In the future, I would like to apply this kMC method to interpret the atomistic DFT data with regard to practical reaction conditions (concentration, temperature, pressure) to calculate reaction rate, selectivity, and the rate determining step. In addition, I want to apply the kMC method for

various rutile surfaces such as IrO_2, RhO_2, PdO_2, PtO_2, VO_2, TiO_2, RuO_2, SnO_2, and ReO_2 to screen their stability and tendency to form surface vacancies.

5.2 HDO Study with Different Surrogate Molecules

To design novel catalyst for HDO catalysis a careful comparison of HDO reactions with different oxidized molecules should be performed, because different oxygen containing functional groups may be activated with different activation steps. In the future, I suggest studying furan (C_4H_4O) as a next target molecule, because furan is third largest product of the pyrolysis step and contains oxygen as part of an aromatic ring structure. It is anticipated that the removal of oxygen from furan over the RuO_2 and the RuO_2/TiO_2 surfaces may follow the hydrodesulfurization (HDS) pathway of thiophenes (C_4H_4S) on sulphide-based catalysts and a careful comparison may allow to translate the existing knowledge of HDS catalysis to the emerging field of HDO catalysis, The required ring-opening mechanism during furan HDO poses a new challenge and may involve higher energy barriers than the ones present during HDO of acetaldehyde. The purpose of this study is to find a model for the better understanding of the interactions between oxygen containing aromatic hydrocarbons (methylfuran, 5-hydroxymethylfurfural, furfural, and furfuryl alcohol) and the catalytic surface of metal oxide catalysts.

Bibliography

[1] Mortensen, P. M.; Grunwaldt, J.-D.; Jensen, P.; Knudsen, K. G.; Jensen, A. D. A review of catalytic upgrading of bio-oil to engine fuels. *Applied Catalysis A: General* **2011**, *407*, 1–19.

[2] Saidur, R.; Abdelaziz, E.; Demirbas, A.; Hossain, M. S.; Mekhilef, S. A review on biomass as a fuel for boilers. *Renewable and Sustainable Energy Reviews* **2011**, *15*, 2262–2289.

[3] Huber, G. W.; Iborra, S.; Corma, A. Synthesis of transportation fuels from biomass: chemistry, catalysts, and engineering. *Chemical reviews* **2006**, *106*, 4044–98.

[4] Choudhary, T. V.; Phillips, C. B. Renewable fuels via catalytic hydrodeoxygenation. *Applied Catalysis A: General* **2011**, *397*, 1–12.

[5] Hoang, T. Q.; Zhu, X.; Danuthai, T.; Lobban, L. L.; Resasco, D. E.; Mallinson, R. G. Conversion of Glycerol to Alkyl-aromatics over Zeolites. *Energy & Fuels* **2010**, *24*, 3804–3809.

[6] Şenol, O.; Viljava, T.-R.; Krause, A. Hydrodeoxygenation of aliphatic esters on sulphided NiMo/γ-Al2O3 and CoMo/γ-Al2O3 catalyst: The effect of water. *Catalysis Today* **2005**, *106*, 186–189.

[7] Dupont, C.; Lemeur, R.; Daudin, A.; Raybaud, P. Hydrodeoxygenation pathways catalyzed by MoS2 and NiMoS active phases: A DFT study. *Journal of Catalysis* **2011**, *279*, 276–286.

[8] Badawi, M.; Paul, J.-F.; Cristol, S.; Payen, E. Guaiacol derivatives and inhibiting species adsorption over MoS2 and CoMoS catalysts under HDO conditions: A DFT study. *Catalysis Communications* **2011**, *12*, 901–905.

[9] Adjaye, J. D.; Sai P.R. Katikaneni, N. N. B. Catalytic conversion of a biofuel to hydrocarbons: effect of mixtures of HZSM-5 and silica-alumina catalysts on product distribution. *Fuel Processing Technology* **1996**, *48*, 115–143.

[10] Katikaneni, S.; Adjaye, J.; Bakhshi, N. Performance of aluminophosphate molecular sieve catalysts for the production of hydrocarbons from wood-derived and vegetable oils. *Energy & fuels* **1995**, 1065–1078.

[11] Li, N.; Huber, G. W. Aqueous-phase hydrodeoxygenation of sorbitol with Pt/SiO2–Al2O3: Identification of reaction intermediates. *Journal of Catalysis* **2010**, *270*, 48–59.

[12] Chen, L.; Zhu, Y.; Zheng, H.; Zhang, C.; Zhang, B.; Li, Y. Aqueous-phase hydrodeoxygenation of carboxylic acids to alcohols or alkanes over supported Ru catalysts. *Journal of Molecular Catalysis A: Chemical* **2011**, *351*, 217–227.

[13] Chen, L.; Zhu, Y.; Zheng, H.; Zhang, C.; Li, Y. Aqueous-phase hydrodeoxygenation of propanoic acid over the Ru/ZrO2 and Ru–Mo/ZrO2 catalysts. *Applied Catalysis A: General* **2012**, *411-412*, 95–104.

[14] Li, R.; Zhang, M.; Yu, Y. A DFT study on the Cu (111) surface for ethyl acetate synthesis from ethanol dehydrogenation. *Applied Surface Science* **2012**, *258*, 6777–6784.

[15] Resasco, D. E. What Should We Demand from the Catalysts Responsible for Upgrading Biomass Pyrolysis Oil? *The Journal of Physical Chemistry Letters* **2011**, *2*, 2294–2295.

[16] Gangadharan, A.; Shen, M.; Sooknoi, T.; Resasco, D. E.; Mallinson, R. G. Condensation reactions of propanal over CexZr1−xO2 mixed oxide catalysts. *Applied Catalysis A: General* **2010**, *385*, 80–91.

[17] Popa, C.; Offermans, W.; Van Santen, R.; Jansen, A. Ab initio density-functional theory study of NHx dehydrogenation and reverse reactions on the Rh(111) surface. *Physical Review B* **2006**, *74*, 1–10.

[18] Honkala, K.; Hellman, A.; Remediakis, I. N.; Logadottir, A.; Carlsson, A.; Dahl, S.; Christensen, C. H.; Nørskov, J. K. Ammonia synthesis from first-principles calculations. *Science* **2005**, *307*, 555–8.

[19] Grabow, L. C.; Mavrikakis, M. Mechanism of Methanol Synthesis on Cu through CO2 and CO Hydrogenation. *ACS Catalysis* **2011**, *1*, 365–384.

[20] Lu, J.; Behtash, S.; Heyden, A. Theoretical Investigation of the Reaction Mechanism of the Decarboxylation and Decarbonylation of Propanoic Acid on Pd (111) Model Surfaces. *The Journal of Physical Chemistry C* **2012**, *116*, 14328–14341.

[21] Vorotnikov, V.; Mpourmpakis, G.; Vlachos, D. G. DFT Study of Furfural Conversion to Furan, Furfuryl Alcohol, and 2-Methylfuran on Pd(111). *ACS Catalysis* **2012**, *2*, 2496–2504.

[22] Ruinart de Brimont, M.; Dupont, C.; Daudin, a.; Geantet, C.; Raybaud, P. Deoxygenation mechanisms on Ni-promoted MoS2 bulk catalysts: A combined experimental and theoretical study. *Journal of Catalysis* **2012**, *286*, 153–164.

[23] Guo, N.; Caratzoulas, S.; Doren, D. J.; Sandler, S. I.; Vlachos, D. G. A perspective on the modeling of biomass processing. *Energy & Environmental Science* **2012**, *5*, 6703.

[24] Over, H.; Muhler, M. Catalytic CO oxidation over ruthenium—bridging the pressure gap. *Progress in Surface Science* **2003**, *72*, 3–17.

[25] Gao, F.; Goodman, D. W. CO oxidation over ruthenium: identification of the catalytically active phases at near-atmospheric pressures. *Physical chemistry chemical physics : PCCP* **2012**, 6688–6697.

[26] Maris, E.; Davis, R. Hydrogenolysis of glycerol over carbon-supported Ru and Pt catalysts. *Journal of Catalysis* **2007**, *249*, 328–337.

[27] Henderson, M. A.; Zhou, Y.; White, J. M. Polymerization and Decomposition of Acetaldehyde on Ru(00 1). *Journal of the American Chemical Society* **1989**, *111*, 1185–1193.

[28] Wendt, S.; Knapp, M.; Over, H. The role of weakly bound on-top oxygen in the catalytic CO oxidation reaction over RuO2(110). *Journal of the American Chemical Society* **2004**, *126*, 1537–41.

[29] López, N.; Novell-Leruth, G. Rules for selectivity in oxidation processes on RuO2(110). *Physical chemistry chemical physics : PCCP* **2010**, *12*, 12217–22.

[30] Moses, P. G.; Hinnemann, B.; Topsøe, H.; Nørskov, J. K. The effect of Co-promotion on MoS2 catalysts for hydrodesulfurization of thiophene: A density functional study. *Journal of Catalysis* **2009**, *268*, 201–208.

[31] Sholl, D. S.; Steckel, J. A. *Density functional theory: a practical introduction*; 1st ed.; JohnWiley & Sons, Inc.: Hoboken, New Jersey, **2009**, 1-10.

[32] Hafner, J. Ab-Initio simulations of materials using VASP: Density-functional theory and beyond. *Journal of computational chemistry* **2008**, *29*, 2044-2078.

[33] Oppenheimer R, B. M. On the Quantum Theory of Molecules. *Annalen der Physik* **1927**, *84*, 457–484.

[34] Hammer, B.; Hansen, L.; Nørskov, J. Improved adsorption energetics within density-functional theory using revised Perdew-Burke-Ernzerhof functionals. *Physical Review B* **1999**, *59*, 7413–7421.

[35] Kresse, G.; Furthmüller, J. Efficient iterative schemes for ab initio total-energy calculations using a plane-wave basis set. *Physical review. B, Condensed matter* **1996**, *54*, 11169–11186.

[36] Bahn, S. R.; Jacobsen, K. W. An object-oriented scripting interface to a legacy electronic structure code. *Computing in Science & Engineering* **2002**, *4*, 56–66.

[37] Perdew, J. P.; Burke, K.; Ernzerhof, M. Generalized gradient approximation made simple. *Physical Review Letters* **1996**, *77*, 3865–3868.

[38] Chueh, Y.-L.; Hsieh, C.-H.; Chang, M.-T.; Chou, L.-J.; Lao, C. S.; Song, J. H.; Gan, J.-Y.; Wang, Z. L. RuO2 Nanowires and RuO2/TiO2 Core/Shell Nanowires: From Synthesis to Mechanical, Optical, Electrical, and Photoconductive Properties. *Advanced Materials* **2007**, *19*, 143–149.

[39] Pan, Y.; Zhang, H.; Shi, D.; Sun, J.; Du, S.; Liu, F.; Gao, H. Highly Ordered, Millimeter-Scale, Continuous, Single-Crystalline Graphene Monolayer Formed on Ru (0001). *Advanced Materials* **2009**, *21*, 2777–2780.

[40] Monkhorst, H. J.; Pack, J. D. Special points for Brillouin-zone integrations. *Physical Review B* **1976**, *13*, 5188–5192.

[41] Santiago, M.; Kondratenko, V. a.; Kondratenko, E. V.; López, N.; Pérez-Ramírez, J. Mechanistic analysis of direct N2O decomposition and reduction with H2 or NH3 over RuO2. *Applied Catalysis B: Environmental* **2011**, *110*, 33–39.

[42] Fan, C. Y.; Wang, J.; Jacobi, K.; Ertl, G. The oxidation of CO on RuO(110) at room temperature. *The Journal of Chemical Physics* **2001**, *114*, 10058.

[43] Bollinger, M.; Jacobsen, K.; Nørskov, J. Atomic and electronic structure of MoS2 nanoparticles. *Physical Review B* **2003**, *67*, 1–17.

[44] NIST Chemistry WebBook. Thermophysical Properties of Fluid Systems, http://webbook.nist.gov/cgi/fluid.cgi?T=600&PLow=0&PHigh=400&PInc=50&Digits=5&ID=C7732185&Action=Load&Type=IsoTherm&TUnit=K&PUnit=MPa&DUnit=mol%2Fl&HUnit=kJ%2Fmol&WUnit=m%2Fs&VisUnit=uPa*s&STUnit=N%2Fm&RefState=DEF - April, 2012.

[45] WebBook, N. C. NIST Chemistry WebBook. Thermophysical Properties of Fluid Systems, http://webbook.nist.gov/cgi/fluid.cgi?T=600&PLow=0&PHigh=300&PInc=100&Digits=5&ID=C1333740&Action=Load&Type=IsoTherm&TUnit=K&PUnit=MPa&DUnit=mol%2Fl&HUnit=kJ%2Fmol&WUnit=m%2Fs&VisUnit=uPa*s&STUnit=N%2Fm&RefState=DEF - April, 2012.

[46] Reuter, K.; Scheffler, M. Composition and structure of the RuO2(110) surface in an O2 and CO environment: Implications for the catalytic formation of CO2. *Physical Review B* **2003**, *68*, 045407.

[47] Sun, Q.; Reuter, K.; Scheffler, M. Hydrogen adsorption on RuO2(110): Density-functional calculations. *Physical Review B* **2004**, *70*, 1–12.

[48] Wang, J.; Fan, C. Y.; Sun, Q.; Reuter, K.; Jacobi, K.; Scheffler, M.; Ertl, G. Surface coordination chemistry: dihydrogen versus hydride complexes on RuO2(110). *Angewandte Chemie* **2003**, *42*, 2151–4.

[49] Knapp, M.; Crihan, D. Complex interaction of hydrogen with the RuO2 (110) surface. *The Journal of Physical Chemistry C* **2007**, *2*, 5363–5373.

[50] Jacobi, K.; Wang, Y.; Ertl, G. Interaction of hydrogen with RuO2(110) surfaces: activity differences between various oxygen species. *The Journal of Physical Chemistry. B* **2006**, *110*, 6115–22.

[51] Lin, H.-Y.; Chen, Y.-W. The kinetics of H2 adsorption on supported ruthenium catalysts. *Thermochimica Acta* **2004**, *419*, 283–290.

[52] Mei, D.; Karim, A. M.; Wang, Y. Density Functional Theory Study of Acetaldehyde Hydrodeoxygenation on MoO 3. *The Journal of Physical Chemistry C* **2011**, *115*, 8155–8164.

[53] Mars, P.; Van Krevelen, D. W. Oxidations carried out by means of vanadium oxide catalysts. *Chemical Engineering Science* **1954**, *3*, 41–59.

[54] Over, H. Surface chemistry of ruthenium dioxide in heterogeneous catalysis and electrocatalysis: from fundamental to applied research. *Chemical reviews* **2012**, *112*, 3356–426.

[55] Del Rosal, I.; Truflandier, L.; Poteau, R.; Gerber, I. C. A Density Functional Theory Study of Spectroscopic and Thermodynamic Properties of Surfacic Hydrides on Ru (0001) Model Surface: The Influence of the Coordination Modes and the Coverage. *The Journal of Physical Chemistry C* **2011**, *115*, 2169–2178.

[56] Hirschl, R. Hydrogenation of ethylene and formaldehyde on Pt (111) and Pt80Fe20 (111): a density-functional study. *Journal of Catalysis* **2004**, *226*, 273–282.

[57] Delbecq, F.; Vigné, F. Acetaldehyde on Pt(111) and Pt/Sn(111): a DFT study of the adsorption structures and of the vibrational spectra. *The journal of physical chemistry. B* **2005**, *109*, 10797–806.

[58] Mei, D.; Karim, A. M.; Wang, Y. On the Reaction Mechanism of Acetaldehyde Decomposition on Mo(110). *ACS Catalysis* **2012**, *2*, 468–478.

[59] Shekhar, R.; Barteau, M. Adsorption and reaction of aldehydes on Pd surfaces. *The Journal of Physical …* **1997**, *5647*, 7939–7951.

[60] Houtman, C. J.; Barteau, M. A. Divergent pathways of acetaldehyde and ethanol decarbonylation on the Rh(111) surface. *Journal of Catalysis* **1991**, *130*, 528–546.

[61] Shekhar, R.; Barteau, M. Adsorption and reaction of aldehydes on Pd surfaces. *The Journal of Physical …* **1997**, *5647*, 7939–7951.

[62] Panagiotopoulou, P.; Kondarides, D. I.; Verykios, X. E. Mechanistic Study of the Selective Methanation of CO over Ru / TiO 2 Catalyst : Identification of Active Surface Species and Reaction Pathways †. **2011**, 1220–1230.

[63] Starr, D. E.; Bluhm, H. Surface Science CO adsorption and dissociation on Ru (0001) at elevated pressures ⋆. *Surface Science* **2013**, *608*, 241–248.

[64] Ciobica, I. .; F, F.; Van Santen, R. .; Kleyn, A. .; Hafner, J. A theoretical study of CH x chemisorption on the Ru (0001) surface. *Chemical Physics Letters* **1999**, *311*, 185–192.

[65] Cheng, J.; Hu, P.; Ellis, P.; French, S.; Kelly, G.; Lok, C. M. An Energy Descriptor To Quantify Methane Selectivity in Fischer−Tropsch Synthesis: A Density Functional Theory Study. *The Journal of Physical Chemistry C* **2009**, *113*, 8858–8863.

[66] Geerlings, J. J. C.; Zonnevylle, M. C.; De Groot, C. P. M. Studies of the Fischer-Tropsch reaction on Co(0001). *Surface Science* **1991**, *241*, 302–314.

[67] Over, H.; Muhler, M.; Seitsonen, A. P. Comment on “CO oxidation on ruthenium: The nature of the active catalytic surface” by D.W. Goodman, C.H.F. Peden, M.S. Chen. *Surface Science* **2007**, *601*, 5659–5662.

[68] Ciobîcă, I. M.; Kramer, G. J.; Ge, Q.; Neurock, M.; Van Santen, R. a. Mechanisms for Chain Growth in Fischer–Tropsch Synthesis over Ru(0001). *Journal of Catalysis* **2002**, *212*, 136–144.

[69] Mirwald, J. W.; Inderwildi, O. R. Unraveling the Fischer-Tropsch mechanism: a combined DFT and microkinetic investigation of C-C bond formation on Ru. *Physical chemistry chemical physics : PCCP* **2012**, 7028–7031.

[70] Zhuo, M.; Tan, K. F.; Borgna, A.; Saeys, M. Density Functional Theory Study of the CO Insertion Mechanism for Fischer−Tropsch Synthesis over Co Catalysts. *The Journal of Physical Chemistry C* **2009**, *113*, 8357–8365.

[71] Hess, F.; Farkas, A.; Seitsonen, A. P.; Over, H. “First-Principles” kinetic monte carlo simulations revisited: CO oxidation over RuO(2) (110). *Journal of computational chemistry* **2012**, *2*, 1–10.

[72] Goodman, D. W.; Peden, C. H. F.; Chen, M. S. CO oxidation on ruthenium: The nature of the active catalytic surface. *Surface Science* **2007**, *601*, L124–L126.

[73] Dhakad, M.; Rayalu, S.; Subrt, J. Diesel soot oxidation on titania-supported ruthenia catalysts. *Current Science* **2007**, *92*, 1125–1128.

[74] Kundu, S.; Vidal, A. B.; Yang, F.; Ramírez, P. J.; Senanayake, S. D.; Stacchiola, D.; Evans, J.; Liu, P.; Rodriguez, J. A. Special Chemical Properties of RuO. **2012**, *2*.

[75] Chatterjee, A.; Vlachos, D. G. An overview of spatial microscopic and accelerated kinetic Monte Carlo methods. *Journal of Computer-Aided Materials Design* **2007**, *14*, 253–308.

[76] Reuter, K.; Frenkel, D.; Scheffler, M. The Steady State of Heterogeneous Catalysis, Studied by First-Principles Statistical Mechanics. *Physical Review Letters* **2004**, *93*, 116105.

Appendix

Table S1. Extra reaction pathway for O-vacancy formation and HDO of CH_3CHO on the $RuO_2(110)$.

no.	Reaction	E_a / eV	ΔE / eV	ν / cm^{-1}
O12	$H_{2(g)} + O^{br} \rightarrow H_2O^{br}*$	2.13	-0.21	935.9i
O13	$H_{2(g)} + O\text{-}H^{br}* + O^{br}* \rightarrow H_2O^{br}* + O\text{-}H^{br}*$	1.87	-0.43	1427.8i
O14	$CH_3CHO*\text{-}s \rightarrow Ru\text{-}CH_3^{cus}* + CHO*\text{-}d$	1.52	1.40	187.6i
O15	$CH_3CHO*\text{-}s \rightarrow CH_3CO*\text{-}s + Ru\text{-}H^{cus}*$	1.94	1.78	357.6i
O16	$CH_3CHO*\text{-}s \rightarrow CH_2CHO*\text{-}s + Ru\text{-}H^{cus}*$	1.08	0.55	872.1i
O17[a]	$CH_3CHO*\text{-}s \rightarrow CH_2CH_{2(g)} + O^{br}*$	2.18	0.12	1092.1i
O18	$CH_3CHO*\text{-}d \rightarrow Ru\text{-}CH_3^{cus}* + CHO*\text{-}d$	1.46	1.33	187.6i
O19	$CH_3CHO*\text{-}d \rightarrow CH_3CO*\text{-}d + O\text{-}H^{br}*$	0.90	0.67	543.1i
O20	$CH_3CHO*\text{-}d + Ru^{cus} \rightarrow CH_2CHO*\text{-}s + Ru\text{-}H^{cus}*$	0.90	0.49	880.2i
O21[b]	$CH_3CO*\text{-}d + Ru^{cus} \rightarrow Ru\text{-}CH_3CO^{cus}*$	0.49	0.15	107.8i
O22	$Ru\text{-}CH_3CO^{cus}* + Ru^{cus} \rightarrow Ru\text{-}CH_3^{cus}* + Ru\text{-}CO^{cus}*$	1.29	-0.34	533.4i
O23	$CH_3CO*\text{-}d + Ru^{cus} \rightarrow Ru\text{-}CH_3C^{cus}* + O^{br}*$	1.58	1.1	367.8i
O24	$CH_3CO*\text{-}d + Ru^{cus} \rightarrow CH_2CO*\text{-}d + Ru\text{-}H^{cus}*$	1.86	1.24	773.9i
O25	$Ru\text{-}CH_3CH^{cus}* + O^{br} \rightarrow O\text{-}CH_3^{br}* + Ru\text{-}CH^{cus}*$	3.60	1.59	359.5i
O26	$Ru\text{-}CH_3CH^{cus}* + O^{br} \rightarrow Ru\text{-}CH_3C^{cus}* + O\text{-}H^{br}*$	0.98	0.25	1429.6i
O27[c]	$Ru\text{-}CH_3CH^{cus}* \rightarrow Ru^{cus} + CH_2CH_{2(g)}$	1.38	-0.27	1035.8i
O28[d]	$CH_2CHO*\text{-}s \rightarrow CH_2CHO*\text{-}d$	0.08	-0.1	35.5i
O29	$CH_2CHO*\text{-}d + Ru^{cus} \rightarrow Ru\text{-}CH_2^{cus}* + CHO*\text{-}d$	2.58	1.91	415.4i
O30	$CH_2CHO*\text{-}d \rightarrow Ru\text{-}CH_2CH^{cus}* + O^{br}*$	1.74	0.84	313.9i
O31	$CH_2CHO*\text{-}d \rightarrow CH_2CO*\text{-}d + Ru\text{-}H^{cus}*$	1.61	1.21	420.0i
O32	$CH_2CHO*\text{-}d + O^{3f} \rightarrow CHCHO*\text{-}d + O\text{-}H^{3f}*$	1.62	0.54	1488.2i
O33	$CH_2CHO*\text{-}d + Ru\text{-}H^{cus}* \rightarrow CH_2CH_{2(g)} + O^{br}*$	1.16	-0.16	355.8i
O34	$Ru\text{-}CH_2CH^{cus}* + Ru^{cus} \rightarrow Ru\text{-}CH_2^{cus}* + Ru\text{-}CH^{cus}*$	2.79	2.72	103.0i
O35	$Ru\text{-}CH_2CH^{cus}* + O^{3f} \rightarrow Ru\text{-}CH_2C^{cus}* + O\text{-}H^{3f}*$	1.88	0.66	1570.1i
O36	$Ru\text{-}CH_2CH^{cus}* + O^{3f} \rightarrow Ru\text{-}CHCH^{cus}* + O\text{-}H^{3f}*$	2.3	1.64	1370.5i

- ΔE and E_a are the total energy change and activation energy barriers without ZPE correction.
- ν denotes the frequency of the imaginary mode at the transition state.
- [a] O14 is intramolecular diffusion of H atom in CH_3CHO* intermediate.
- [b] O18 is diffusion of CH_3CO*-d intermediate from bidentate configuration to Ru^{cus} site.
- [c] O24 is intramolecular diffusion of H atom in CH_3CH* intermediate.
- [d] O25 is transformation of CH_2CHO*-s to bidentate configuration of CH_2CHO*-d.

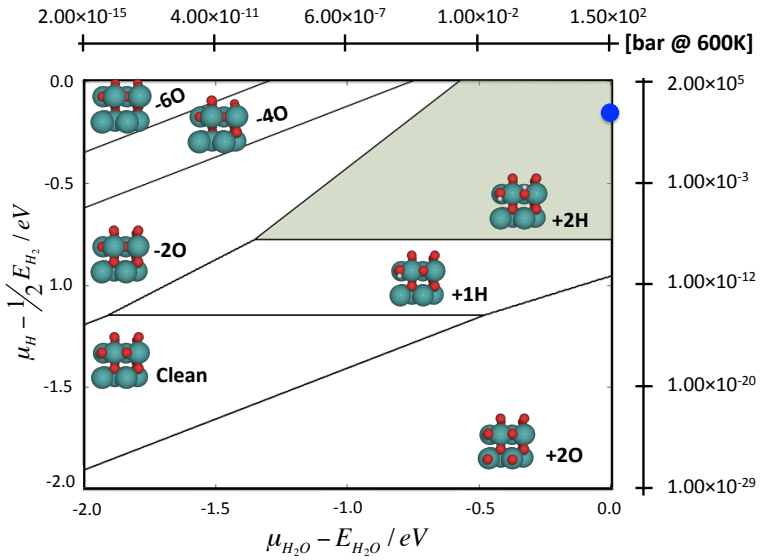

S. 1. Phase diagram of the RuO_2(110) - p(2×2) surface (white – hydrogen / red – oxygen / teal – ruthenium). Thermodynamic data for chemical potentials were taken from NIST [reference 45 in manuscript]. The moss green represents the equilibrated RuO_2 (110) surface at given HDO reaction conditions (T > 500 K, p_{H_2} > 200 bar) and specifically the blue circle denotes chemical potentials at T = 600 K and p_{H_2} = 200 bar.

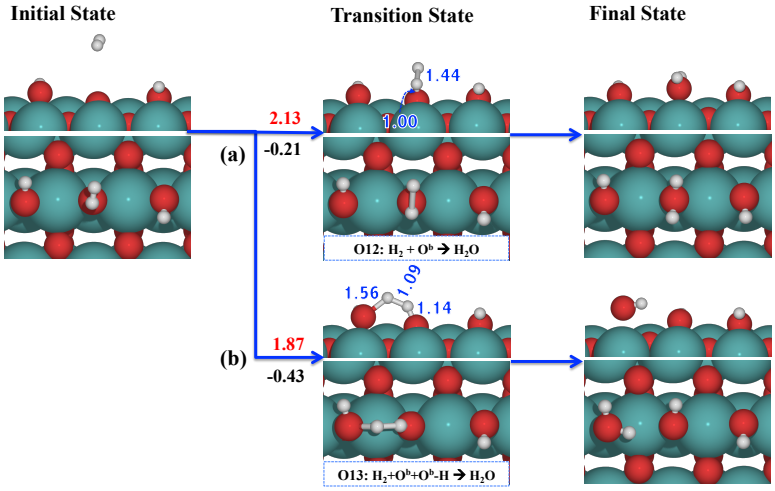

S. 2. Calculated reaction pathways of O-vacancy formation (white – hydrogen / red – oxygen / teal – ruthenium). Numerical values in red, black and blue represent the activation energy barrier E_a [eV], the reaction energy ΔE [eV] and bond distance [Å], respectively. (a) Reaction O12: $H_{2(g)} + O^{br} \rightarrow H_2O^{br}*$, O11; (b) Reaction O13: $H_{2(g)}$ + O-$H^{br}*$ + $O^{br}*\rightarrow$ $H_2O^{br}*$ + O-$H^{br}*$.

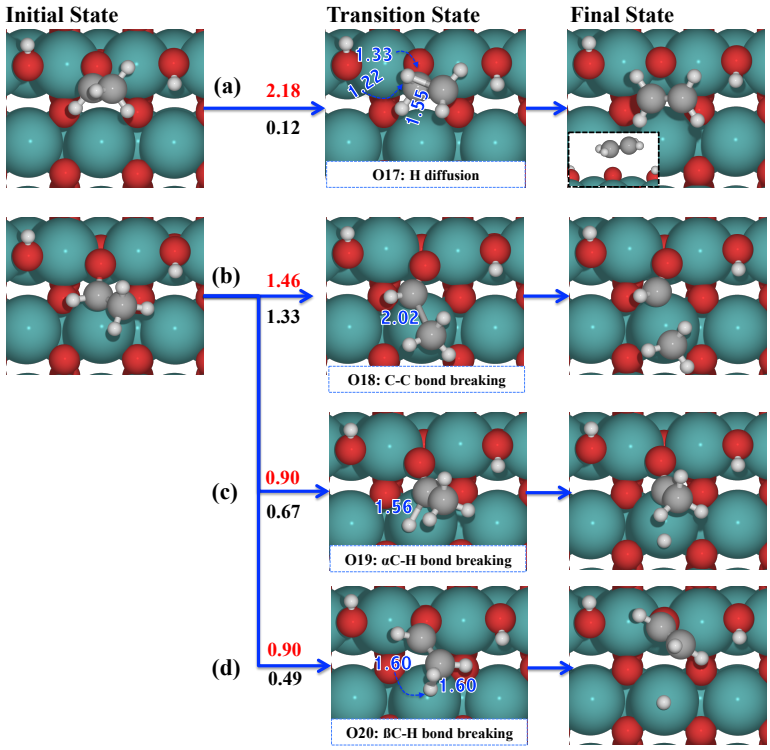

S. 3. Calculated reaction pathway of CH_3CHO HDO on $RuO_2(110)$ (white – hydrogen / red – oxygen / gray – carbon / teal – ruthenium). Numerical values in red, black and blue represent the activation energy barrier E_a [eV], the reaction energy ΔE [eV] and bond distance [Å], respectively. (a) Reaction O17: CH_3CHO*-s → $CH_2CH_{2(g)}$ + O^{br}*; (b) Reaction O18: CH_3CHO*-d → Ru-CH_3^{cus}* + CHO*-d; (c) Reaction O19: CH_3CHO*-d → CH_3CO*-d + O-H^{br}*; (d) Reaction O20: CH_3CHO*-d + Ru^{cus} → CH_2CHO*-s + Ru-H^{cus}*.

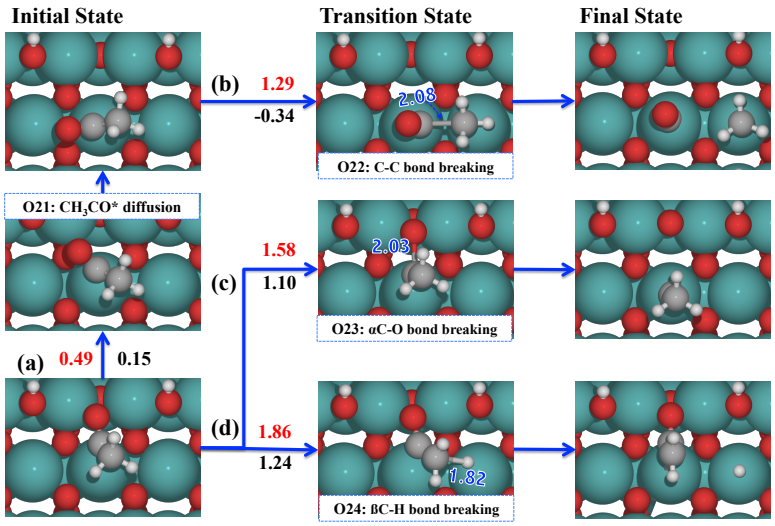

S. 4. Calculated reaction pathway of CH_3CHO HDO on $RuO_2(110)$ (white – hydrogen / red – oxygen / gray – carbon / teal – ruthenium). Numerical values in red, black and blue represent the activation energy barrier E_a [eV], the reaction energy ΔE [eV] and bond distance [Å], respectively. (a) Reaction O21: CH_3CO*-d + Ru^{cus}→ Ru-CH_3CO^{cus}*; (b) Reaction O22: Ru-CH_3CO^{cus}* + Ru^{cus} → Ru-CH_3^{cus}* + Ru-CO^{cus}*; (c) Reaction O23: CH_3CO*-d+ Ru^{cus} → Ru-CH_3C^{cus}* + O^{br}*; (d) Reaction O24: CH_3CO*-d + Ru^{cus} → CH_2CO*-d + Ru-H^{cus}*.

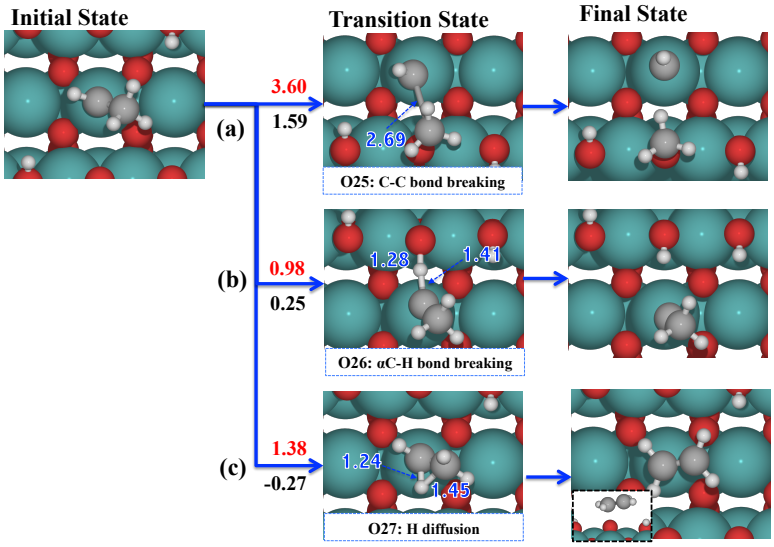

S. 5. Calculated reaction pathway of CH_3CHO HDO on $RuO_2(110)$ (white – hydrogen / red – oxygen / gray – carbon / teal – ruthenium). Numerical values in red, black and blue represent the activation energy barrier E_a [eV], the reaction energy ΔE [eV] and bond distance [Å], respectively. (a) Reaction O25: Ru-CH_3CH^{cus}* + O^{br} → O-CH_3^{br}* + Ru-CH^{cus}*; (b) Reaction O26: Ru-CH_3CH^{cus}* + O^{br} → Ru-CH_3C^{cus}* + O-H^{br}*; (c) Reaction O27: Ru-CH_3CH^{cus}* → Ru^{cus} + $CH_2CH_{2(g)}$.

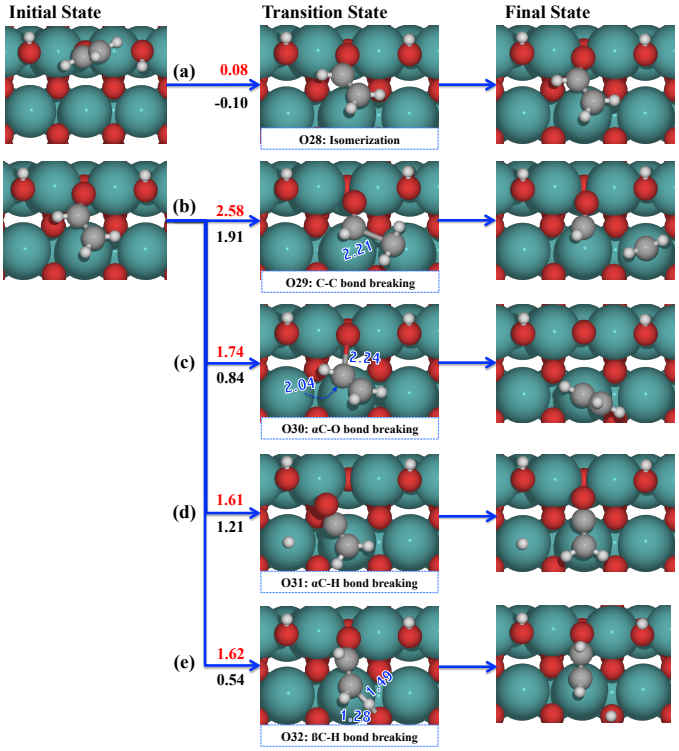

S. 6. Calculated reaction pathway of CH_3CHO HDO on $RuO_2(110)$ (white – hydrogen / red – oxygen / gray – carbon / teal – ruthenium). Numerical values in red, black and blue represent the activation energy barrier E_a [eV], the reaction energy ΔE [eV] and bond distance [Å], respectively. (a) Reaction O28: CH_2CHO*-s → CH_2CHO*-d; (b) Reaction O29: CH_2CHO*-d + Ru^{cus} → Ru-CH_2^{cus}* + CHO*-d; (c) Reaction O30: CH_2CHO*-d → Ru-CH_2CH^{cus}* + O^{br}*; (d) Reaction O31: CH_2CHO*-d → CH_2CO*-d + Ru-H^{cus}*; (e) Reaction O32: CH_2CHO*-d + O^{3f} → CHCHO*-d + O-H^{3f}*.

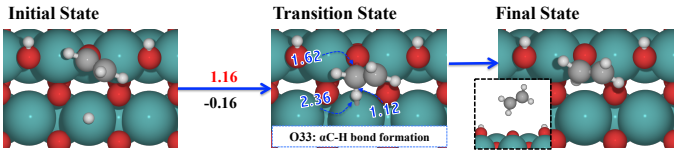

S. 7. Calculated reaction pathway of CH_3CHO HDO on $RuO_2(110)$ (white – hydrogen / red – oxygen / gray – carbon / teal – ruthenium). Numerical values in red, black and blue represent the activation energy barrier E_a [eV], the reaction energy ΔE [eV] and bond distance [Å], respectively. Reaction O33: CH_2CHO*-d + Ru-H^{cus}* → $CH_2CH_{2(g)}$ + O^{br}*.

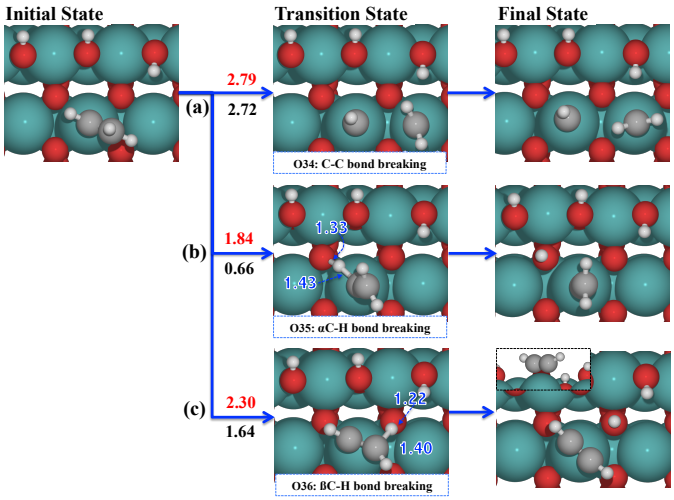

S. 8 Calculated reaction pathway of CH_3CHO HDO on $RuO_2(110)$ (white – hydrogen / red – oxygen / gray – carbon / teal – ruthenium). Numerical values in red, black and blue represent the activation energy barrier Ea [eV], the reaction energy ΔE [eV] and bond distance [Å], respectively. (a) Reaction O34: Ru-CH_2CH^{cus}* + Ru^{cus}→ Ru-CH_2^{cus}* + Ru-CH^{cus}*; (b) Reaction O35: Ru-CH_2CH^{cus}* + O^{3f} → Ru-CH_2C^{cus}* + O-H^{3f}*; (c) Reaction O36: Ru-CH_2CH^{cus}* + O3f → Ru-$CHCH^{cus}$* + O-H^{3f}*, final product of this reaction is acetylene (HC≡CH) on Rucus.

Table S2. Extra reaction pathway for CH_3CHO HDO on the Ru(0001) surface.

no.	Reaction	E_a / eV	ΔE / eV	ν / cm^{-1}
M19	$CH_3CHO^* \rightarrow CH_3^* + CHO^*$	1.10	0.46	380.5i
M20	$CH_3CHO^* \rightarrow CH_3CH^*+O^*$	0.91	-0.77	405.1i
M21	$CH_3CO^* \rightarrow CH_3^* + CO^*$	1.11	-0.44	381.3i
M22	$CH_3CO^* \rightarrow CH_3C^* + O^*$	1.06	-0.89	52.9i
M23	$CH_3C^* \rightarrow CH_3^* + C^*$	1.84	3.67	172.7i
M24	$CH_3C^* \rightarrow CH_2C^* + H^*$	0.80	0.06	854.2i
M25	$CH_2C^* \rightarrow CH_2^* + C^*$	1.89	3.39	338.8i
M26	$CH_2C^* \rightarrow CHC^* + H^*$	1.04	0.05	754.7i
M27	$CHC^* \rightarrow CC^* + H^*$	1.53	0.70	1074i
M28	$CH_2CHO^* \rightarrow CH_2^* + CHO^*$	0.97	0.67	348.3i
M29	$CH_2CHO^* \rightarrow CH_2CH^* + O^*$	1.32	-0.70	446.0i
M30	$CH_2CHO^* \rightarrow CHCHO^* + H^*$	0.61	-0.52	651.2i
M31	$CH_2CO^* \rightarrow CH_2C^* + O^*$	1.44	-0.81	506.6i
M32	$CH_2CO^* \rightarrow CHCO^* + H^*$	0.75	-0.34	906.5i

- ΔE and E_a are the total energy change and activation energy barriers without ZPE correction.
- ν denotes the frequency of the imaginary mode at the transition state.

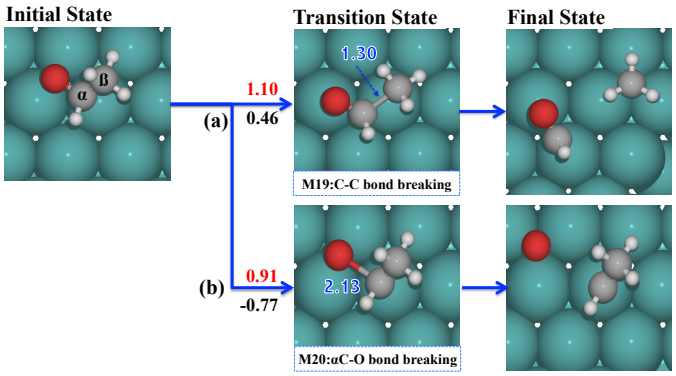

S. 9. Calculated reaction pathway of CH_3CHO HDO on Ru(0001) (white – hydrogen / red – oxygen / gray – carbon / teal – ruthenium). Numerical values in red, black and blue represent the activation energy barrier E_a [eV], the reaction energy ΔE [eV] and bond distance [Å], respectively. (a) Reaction M19: $CH_3CHO^* \rightarrow CH_3^* + CHO^*$; (b) Reaction M20: $CH_3CHO^* \rightarrow CH_3CH^* + O^*$.

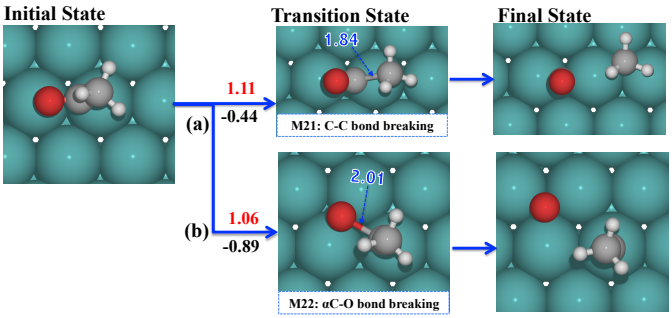

S. 10. Calculated reaction pathway of CH_3CHO HDO on Ru(0001) (white – hydrogen / red – oxygen / gray – carbon / teal – ruthenium). Numerical values in red, black and blue represent the activation energy barrier E_a [eV], the reaction energy ΔE [eV] and bond distance [Å], respectively. (a) Reaction M21: $CH_3CO^* \rightarrow CH_3^* + CO^*$; (b) Reaction M22: $CH_3CO^* \rightarrow CH_3C^* + O^*$.

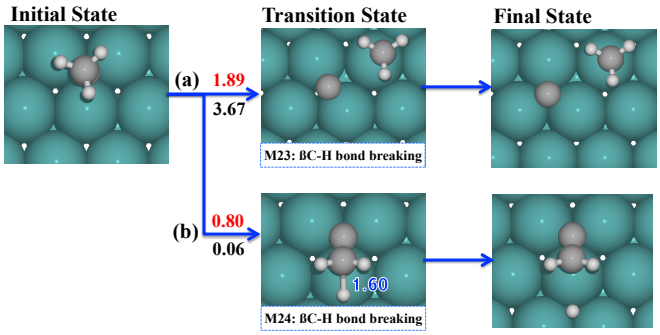

S. 11 Calculated reaction pathway of CH_3CHO HDO on Ru(0001) (white – hydrogen / gray – carbon / teal – ruthenium). Numerical values in red, black and blue represent the activation energy barrier E_a [eV], the reaction energy ΔE [eV] and bond distance [Å], respectively. (a) Reaction M23: $CH_3C^* \rightarrow CH_3^* + C^*$; (b) Reaction M24: $CH_3C^* \rightarrow CH_2C^* + H^*$.

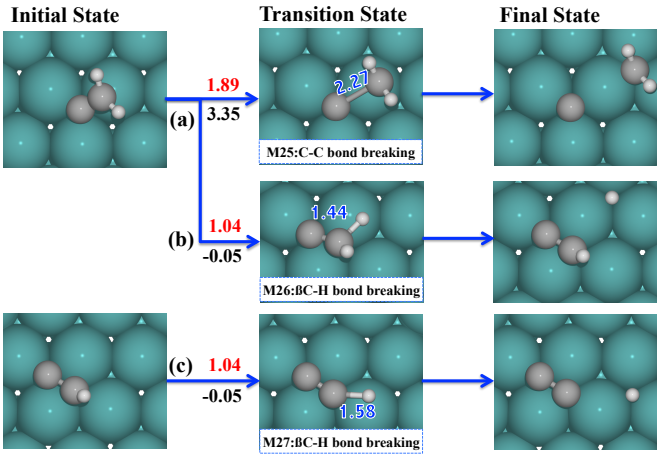

S. 12. Calculated reaction pathway of CH_3CHO HDO on Ru(0001) (white – hydrogen / gray – carbon / teal – ruthenium). Numerical values in red, black and blue represent the activation energy barrier E_a [eV], the reaction energy ΔE [eV] and bond distance [Å], respectively. (a) Reaction 25: $CH_2C^* \rightarrow CH_2^* + C^*$; (d) Reaction 26: $CH_2C^* \rightarrow CHC^* + H^*$; (e) Reaction 27: $CHC^* \rightarrow CC^* + H^*$.

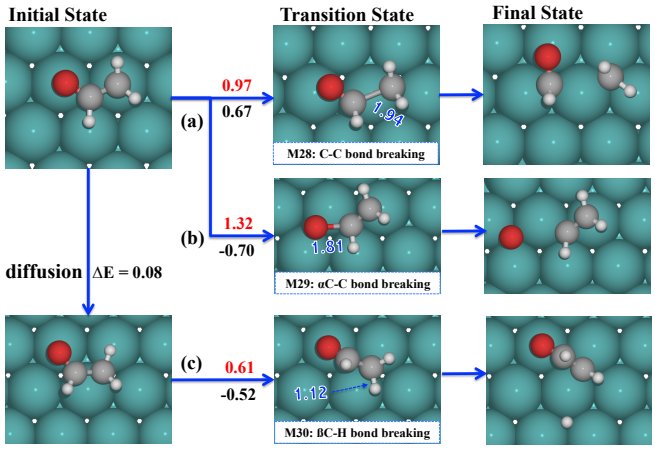

S. 13. Calculated reaction pathway of CH_3CHO HDO on Ru(0001) (white – hydrogen / red – oxygen / gray – carbon / teal – ruthenium). Numerical values in red, black and blue represent the activation energy barrier E_a [eV], the reaction energy ΔE [eV] and bond distance [Å], respectively. (a) Reaction M28: $CH_2CHO^* \rightarrow CH_2^* + CHO^*$; (b) Reaction M29: $CH_2CHO^* \rightarrow CH_2CH^* + O^*$; (c) Reaction M30: $CH_2CHO^* \rightarrow CHCHO^* + H^*$, ΔE of diffusion is 0.08 eV before this reaction.

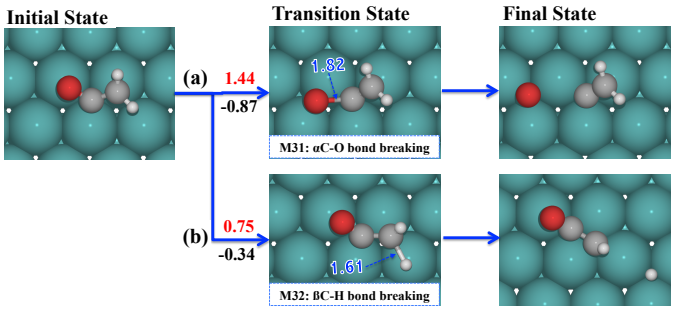

S. 14. Calculated reaction pathway of CH_3CHO HDO on Ru(0001) (white – hydrogen / red – oxygen / gray – carbon / teal – ruthenium). Numerical values in red, black and blue represent the activation energy barrier E_a [eV], the reaction energy ΔE [eV] and bond distance [Å], respectively. (a) Reaction M31: $CH_2CO^* \rightarrow CH_2C^* + O^*$; (b) Reaction M32: $CH_2CO^* \rightarrow CHCO^* + H^*$.

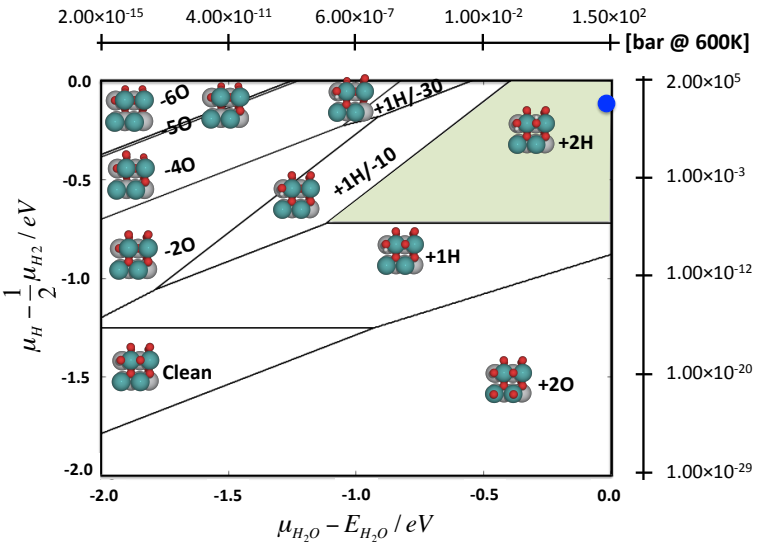

S. 15. Phase diagram of the $RuO_2/TiO_2(110)$ - p(2×2) surface (white – hydrogen / red – oxygen / gray – titanium / teal – ruthenium). Thermodynamic data for chemical potentials were taken from NIST [reference 45 in manuscript]. The moss green represents the equilibrated $RuO_2/TiO_2(110)$ surface at given HDO reaction conditions (T > 500 K, p_{H_2} > 200 bar) and specifically the blue circle denotes chemical potentials at T = 600 K and p_{H_2} = 200 bar.